Journal of Quantitative Spectroscopy & Radiative Transfer ▮ (▮▮▮▮) ▮▮▮–▮▮▮

Contents lists available at ScienceDirect

Journal of Quantitative Spectroscopy & Radiative Transfer

journal homepage: www.elsevier.com/locate/jqsrt

The Monte Carlo atmospheric radiative transfer model McArtim: Introduction and validation of Jacobians and 3D features

Tim Deutschmann [a,*], Steffen Beirle [b], Udo Frieß [a], Michael Grzegorski [b], Christoph Kern [a,1], Lena Kritten [a], Ulrich Platt [a], Cristina Prados-Román [a], Jānis Puķīte [b], Thomas Wagner [b], Bodo Werner [a], Klaus Pfeilsticker [a]

[a] Institute for Environmental Physics, Im Neuenheimer Feld 229, 69120 Heidelberg, Germany
[b] Max-Planck Institute for Chemistry, Joh.-Joachim-Becher-Weg 27, 55128 Mainz, Germany

ARTICLE INFO

Article history:
Received 5 August 2010
Received in revised form
21 December 2010
Accepted 22 December 2010

Keywords:
Radiative transfer equation
Neumann series
Theorem of optical mutuality
Monte Carlo method
3D radiative transfer
Jacobians

ABSTRACT

A new Monte Carlo atmospheric radiative transfer model is presented which is designed to support the interpretation of UV/vis/near-IR spectroscopic measurements of scattered Sun light in the atmosphere. The integro differential equation describing the underlying transport process and its formal solution are discussed. A stochastic approach to solve the differential equation, the Monte Carlo method, is deduced and its application to the formal solution is demonstrated. It is shown how model photon trajectories of the resulting ray tracing algorithm are used to estimate functionals of the radiation field such as radiances, actinic fluxes and light path integrals. In addition, Jacobians of the former quantities with respect to optical parameters of the atmosphere are analyzed. Model output quantities are validated against measurements, by self-consistency tests and through inter comparisons with other radiative transfer models.

1. Introduction

Radiative transfer modeling (RTM) is the numerical prediction of quantities related to the radiative energy transfer in a medium such as the Earth's atmosphere. Examples of these quantities are irradiances, radiances, radiative heating rates and actinic fluxes the latter needed for photochemical modeling. Certain light path integrals, e.g. of the trace gas number density are also often needed in remote sensing applications. Particularly in the interpretation of spectral radiances measured by passive remote sensing instruments, RTM plays a key role. In the early years, many of the numerical methods applied to simulate the transport of electromagnetic radiation were developed in the context of neutron transport modeling. Amongst other algorithms such as the discrete ordinate methods ([1,2] and later [3,4]), the Monte Carlo method developed by Metropolis and Ulam [5] and later applied to problems of atmospheric radiation by Marchuk et al. [6] has established itself as an unbiased and possibly as the most flexible method (e.g. [7–13]. For a review on various RT models see [14]).

This paper introduces the radiative transfer program McArtim (Monte Carlo atmospheric radiative transfer inversion model) that has been developed in order to support the interpretation of spectroscopic data gained in remote sensing applications. McArtim is the successor of the RTM TRACY-II of which some features were already validated by Wagner et al. [15]. TRACY-II is a reimplementation merely following the ideas of TRACY-I [16]. Although McArtim contains parts of the code of TRACY-II, McArtim is in many ways a new implementation and uses a somewhat different approach.

Specifically, in order to reconstruct the state of the atmosphere, e.g. to retrieve profiles of trace gas number densities or aerosol extinction coefficients, McArtim predicts

* Corresponding author. Tel.: +49 6221 546318.
E-mail address: Tim.Deutschmann@iup.uni-heidelberg.de (T. Deutschmann).
[1] Now at U.S. Geological Survey, Cascades Volcano Observatory, 1300 SE Cardinal Court, Vancouver, Washington 98683, USA.

0022-4073/$ - see front matter © 2011 Elsevier Ltd. All rights reserved.
doi:10.1016/j.jqsrt.2010.12.009

the outcome of spectroscopic measurements given a certain state vector. Hence, McArtim is a forward model in the context of mathematical inversion. Quantities of particular interest for inversion are Jacobians of the measured quantities (radiances and light path integrals) with respect to the state vector that is retrieved, and also the radiometric quantities themselves. Recent publications address this topic by means of, e.g., retrieving trace gas concentration profiles using the optical properties of the aerosols present in the atmosphere as constraints [17,18].

For UV/vis/near-IR applications, a well known spectroscopic analysis technique is the differential optical absorption spectroscopy (DOAS) method [19–22]. DOAS can be used to infer light path integrals of trace gas number densities (so-called slant column densities or SCDs) from the ratio of measured spectra versus a background spectrum. Spatial distributions of trace gas concentrations can be obtained from a set of SCDs measured from a moving platform and/or in different viewing directions (see e.g. [18,23–25]). By additionally measuring the absorption of species with known atmospheric concentrations such as O^2 or the oxygen collisional dimer O_4, optical properties of the atmosphere and its constituents like clouds and aerosols, such as photon path length distributions [26–28] and profiles of boundary layer aerosols can be inferred [29–33]. Another promising extension in the remote sensing of aerosols in combination with RTM is to detect the degree of polarization of the scattered light (see [34–36]).

The purpose of the present study is to describe and to report on the major features of McArtim and to discuss validation exercises performed with observations and RT modeling of test cases of the I3RC (Inter comparison of 3D Radiation Codes) workshop [37]. The I3RC provides a benchmarking framework for 3D radiation codes. The knowledge gained throughout the I3RC workshop has been put together into a 3D radiation code available to the public [38]. Furthermore the paper aims at presenting theory and implementation of a scalar Monte Carlo RTM in a more compact form than already available. For example in the pioneering work [6] an explicit expression for the initial collision density was not given. In the book of Marshak and Davis [11], its derivation is fragmented over large text parts and also differs from Marchuk's definition. Additionally, the paper discusses two to some extent novel aspects that have not been presented in the literature in detail: ray tracing on spherical three dimensional grids and the aforementioned radiance and Jacobians light path integral obtained through Monte Carlo RTM.

The paper is organized as follows: Section 2 introduces the underlying physics in form of the integro differential equation for radiative transfer (RTE) and discusses the boundary conditions (i.e. the sources of electro-magnetic radiation). An integral form, the IRTE, is deduced and solved using a *Neumann* series. The *Neumann* series deduced in the paper represents the solution of the RTE in terms of the collision density and is the basis of the Monte Carlo methods. The collision density is the product of the radiance at a certain location and in a certain direction with the local extinction coefficient. Estimates of the *Neumann* series are obtained by randomly sampling light paths (or *path generation*, see Section 3) e.g. occurring during a spectroscopic radiance measurement. Further Jacobians of functionals of the RTE solution are calculated from a trajectory ensemble by applying the method of dependent sampling (Section 4). Section 5 reports on validation exercises based on synthetic observations, balloon borne measurements of relative radiances and I3RC examples.

Table 1 shows a glossary of frequently used terms and symbols in the paper.

Table 1
Terms, abbreviations and symbols used in the paper.

Symbol	Meaning	Unit
VRTE, RTE (SRTE)	Vector, scalar radiative transfer equation	–
DOAS	Differential optical absorption spectroscopy	
$\vec{r}$, $\vec{\omega}$	Location, direction	$\vec{\text{km}}$,1
$\sigma_x(\lambda)$, $n_x(\vec{r})$	Cross section, number density of constituent x	cm^2, cm^{-3}
ε, $\varepsilon_a(\beta)$, ε_s	Extinction, absorption and scattering coefficient	km^{-1}
ϖ_0	Single scattering albedo	1
$\mu=\vec{\omega}_1\vec{\omega}_2=\cos(\theta_{12})$	Cosine of angle between $\vec{\omega}_1$ and $\vec{\omega}_2$	1
$P(\vec{r},\mu)$	Phase function	sr^{-1}
$I(\vec{r},\vec{\omega})$, $B(T,\lambda)$	Radiance, Planck function	W/m^2 sr μm
$S(\vec{r})$, $f(\vec{r},\vec{\omega})$, $\Psi(\vec{r},\vec{\omega})$	Photon source, collision, initial collision density	W/m^3 sr μm
$P_0(\lambda)$	Spectral emissivity power	W/μm
$k_p^{(\dagger)}[(\vec{r},\vec{\omega})\overset{(\leftarrow)}{\rightarrow}(\vec{r}',\vec{\omega}')]$	(Adjoint) transition density	km^{-1}
$K^{(\dagger)}$	(Adjoint) transition density operator	1
O_{rt}	Operator replacing the right side of the IRTE	1
SZA, SRAA	Solar zenith, relative azimuth angle	deg
ZA, VA	Zenith, viewing azimuth angle	deg
RRS	Rotational Raman scattering	–
CDF, PDF	Cumulative, probability density function	1, dep.
T, p	Temperature, pressure	K, hPa
FOV, LOS	Field of view, line of sight	–
MFP, FPL	Mean free path, free path length	km

Please cite this article as: Deutschmann T, et al. The Monte Carlo atmospheric radiative transfer model McArtim: Introduction and validation of Jacobians and 3D features. JQSRT (2011), doi:10.1016/j.jqsrt.2010.12.009

2. The monochromatic unpolarized (scalar) equation of radiation transfer

The vector RTE (VRTE) fully describing the polarized electromagnetic field in a medium can be derived from the Maxwell equations (e.g., [39,40] and [41, Section 8.11]. In its scalar approximation, which is obtained by replacing the vectors and matrices by their first, respectively, (1,1) elements, the RTE rather describes the propagation of non-interfering single velocity particles and neglects especially the polarization of the EM field. Accordingly it is not surprising that when comparing measurements of the physical characteristics of the radiation field (here the specific polarized radiance) to predictions from a scalar RTM, differences of the order of up to 10% can be found for purely Rayleigh scattering atmospheres [42]. However, for many atmospheric conditions, especially in the presence of cloud or aerosol particles, these deviations are small and the scalar approach is accurate.

Over the past decades a certain terminology has been established in the field of scalar radiative transfer modeling. The 2009 paper of Mishchenko [43] analyzes the problematic vocabulary and gives recommendations on how to avoid conflicts with fundamental physical principles. Bearing the assumptions of the scalar approach in mind, we will use terms and expressions that developed in the context of Monte Carlo radiative transfer modeling implying the aforementioned corpuscle character of the model photons. It has to be emphasized that the methods used as, for instance, the decomposition of the radiation field into orders of scattering, the probabilistic description of the transport process as well as the terms like "photon trajectory" have a purely mathematical origin in the context of Monte Carlo RT modeling. With respect to the largest simplification made, the neglect of polarization, it has to be emphasized that the resulting trajectory ensembles can be used nevertheless to obtain the polarized EM fields by retrospectively considering the vector nature of the RT process. This has recently been demonstrated by Cornet et al. [35] and Emde et al. [36].

The monochromatic scalar radiative transfer equation, which describes the gradient of the radiance $I(\vec{r},\vec{\omega})$ at the position $\vec{r}$ in the direction $\vec{\omega}$ is given by

$$\vec{\omega}\,\vec{\nabla} I(\vec{r},\vec{\omega}) = -\varepsilon(\vec{r}) I(\vec{r},\vec{\omega}) + \frac{\varepsilon_s(\vec{r})}{4\pi}\int_{4\pi} I(\vec{r},\vec{\omega}') P(\vec{r},\vec{\omega}\cdot\vec{\omega}')\, d\vec{\omega}' + S(\vec{r}). \quad (1)$$

The first term on the right side describes the differential attenuation of light by extinction with the coefficient $\varepsilon(\vec{r})$. In the scalar approximation, it is assumed that the extinction coefficient is isotropic and homogeneous. Note that in general, the isotropy is violated since, for instance, falling rain drops or ice particles tend to be oriented resulting in a direction dependency of their optical parameters. The second term collects the scattered radiance at $\vec{r}$ by integration over all directions, where $\varepsilon_s(\vec{r})$ denotes the scattering coefficient and $P(\vec{r},\mu)$ is the effective phase function of the medium at the location $\vec{r}$ evaluated with the cosine of the scatter angle $\mu=\cos(\vartheta)$. 4π in the denominator of the factor results from the normalization of the phase function. Again, in the scalar approach the phase functions are assumed to be independent on the particle orientation. The last term $S(\vec{r})$ in Eq. (1) is the so-called source density,

$$S(\vec{r}) = \varepsilon_a(\vec{r}) B_T(\vec{r},\lambda) + P_0(\lambda)\Theta_{\mathrm{Sun}}(\vec{r}) + S_{\mathrm{sf}}(\vec{r},\lambda). \quad (2)$$

$S(\vec{r})$ is given by the density of thermally emitted radiation $B_T(\vec{r},\lambda)$ of the Earth's atmosphere with local absorption (emission) coefficient $\varepsilon_a(\vec{r})$, the Earth's thermal surface emission S_{sf} and the Sun, where $P_0(\lambda)$ is the spectral power of the Sun at its surface and

$$\Theta_{\mathrm{Sun}}(\vec{r}) = \begin{cases} \dfrac{3}{4\pi R_{\mathrm{Sun}}^3} & \text{if } \vec{r} \text{ is located in the Sun,} \\ 0 & \text{else.} \end{cases} \quad (3)$$

For sake of completeness it has to be mentioned that the RTE in form of Eq. (1) does not account for inelastic scattering processes (e.g. rotational Raman scattering). A detailed treatment of rotational Raman scattering especially regarding the Ring effect is presented in Vountas et al. [44].

2.1. RTE integral form

In the form given in Eq. (1), the RTE also contains the boundary conditions (BC, in S). Usually, in order to solve a differential equation (DE), the BCs are applied to the general solution of the homogeneous DE so as to define the integration constants. When including the BCs into the DE, the general solution of the inhomogeneous DE is directly obtained by applying Green's function of the homogeneous differential operator to the boundary conditions. A general discussion of this technique can be found in e.g. [45]. The method of Green's function was first applied by Marchuk [6] using results from Vladimirov [46]. Here we discuss the derivation of all important equations related to this issue.

Eq. (1) is rearranged in order to obtain the integral form:

$$\underbrace{\left[1+\frac{1}{\varepsilon(\vec{r})}\vec{\omega}\,\vec{\nabla}\right]}_{=:D} I(\vec{r},\vec{\omega}) = \frac{\varpi_0(\vec{r})}{4\pi}\int_{4\pi} I(\vec{r},\vec{\omega}') P(\vec{r},\vec{\omega}\cdot\vec{\omega}')\, d\vec{\omega}' + \frac{1}{\varepsilon(\vec{r})} S(\vec{r}). \quad (4)$$

The total single scattering albedo $\varpi_0(\vec{r})$ in the equation above is the ratio of scattering and extinction coefficient $\varpi_0(\vec{r}) = \varepsilon_s(\vec{r})/\varepsilon(\vec{r})$. Single scattering albedos usually depend on the orientation of the particles. As before for phase functions and scattering coefficients we assume isotropy. Green's function $G_{\vec{\omega}}(\vec{r},\vec{r}')$ of the operator D can be obtained by considering equation Eq. (4) for points located on a line along the direction $\vec{\omega}$ through $\vec{r}'$. It writes (compare to Marshak and Davis [11, p. 214]):

$$G_{\vec{\omega}}(\vec{r},\vec{r}') = \delta_{\vec{r}}(\vec{r}',\vec{\omega})\frac{\varepsilon(\vec{r}')\exp(-\tau(\vec{r},\vec{r}'))}{|\vec{r}-\vec{r}'|^2}. \quad (5)$$

In Eq. (5) above the δ function

$$\delta_{\vec{r}}(\vec{r}',\vec{\omega}) = \delta\left(\vec{\omega} - \frac{\vec{r}-\vec{r}'}{|\vec{r}-\vec{r}'|}\right). \quad (6)$$

Selects only points $\vec{r}$ on the line $\vec{r}'+t\vec{\omega}$ with $t>0$. The r^{-2} dependency is needed to compensate for factors occurring in a spatial integration with $G_{\vec{\omega}}$ as a kernel. The remaining

factor can be identified as a density of extinction events along the line $\vec{r}'+t\vec{\omega}$, where the optical thickness τ of extinction is defined as

$$\tau(\vec{r},\vec{r}') = \int_0^{|\vec{r}-\vec{r}'|} \varepsilon(\vec{r}'+t\vec{\omega})\, dt. \tag{7}$$

By convoluting both sides of Eq. (4) with $G_{\vec{\omega}}$ and subsequently scaling with $\varepsilon(\vec{r})$, the integral form of the RTE, the IRTE, in terms of the *collision density*, i.e. the product of the radiance with the extinction coefficient, is obtained:

$$\begin{aligned} f(\vec{r},\vec{\omega}) &:= \varepsilon(\vec{r})I(\vec{r},\vec{\omega}) \\ &= \int_M \int_{4\pi} \delta_{\vec{r}}(\vec{r}',\vec{\omega}) \frac{k_p[(\vec{r}',\vec{\omega}')\to(\vec{r},\vec{\omega})]}{|\vec{r}-\vec{r}'|^2} f(\vec{r}',\vec{\omega}')\, d\vec{\omega}'\, d\vec{r}' \\ &\quad + \Psi(\vec{r},\vec{\omega}). \end{aligned} \tag{8}$$

Here the *transition density* is given by

$$\begin{aligned} &k_p[(\vec{r}',\vec{\omega}')\to(\vec{r},\vec{\omega})] \\ &\quad = \varpi_0(\vec{r}') \frac{P(\vec{r}',\vec{\omega}\cdot\vec{\omega}')}{4\pi} \varepsilon(\vec{r}) \exp(-\tau(\vec{r},\vec{r}')) \end{aligned} \tag{9}$$

and the *initial collision density* $\Psi(\vec{r},\vec{\omega})$ is given by

$$\Psi(\vec{r},\vec{\omega}) = \varepsilon(\vec{r}) \int_M \delta_{\vec{r}}(\vec{r}',\vec{\omega}) S(\vec{r}') \frac{\exp(-\tau(\vec{r},\vec{r}'))}{|\vec{r}-\vec{r}'|^2} d\vec{r}'. \tag{10}$$

The transition density k_p in Eq. (9) plays a crucial role in the Monte Carlo ray tracing method described in this paper. It can be interpreted as the probability of a model photon to perform the transition $(\vec{r}',\vec{\omega}')\to(\vec{r},\vec{\omega})$ through an "atomistic" transport process including (a) a scatter event with single scattering albedo ϖ_0 (probability of a model photon to survive an extinction event) and a phase function P (a density of cosines of scatter angles) and (b) a PDF of free path lengths $\varepsilon\exp(-\tau)$. The initial transition density in Eq. (10) is the density of initially interacting (by extinction) radiation after entering the Earth's atmosphere. In both Eqs. (8) and (10) the spatial integrations are carried out over the spatial region M which includes the Earth and the Sun.

Since the thermal emission of the Earth's surface and the atmosphere is small in the UV/vis/NIR spectral range, it is omitted in the following. Instead of $\Psi(\vec{r},\vec{\omega})$ as given in Eq. (10), the normalized (i.e. $P_0(\lambda)=1$) expression

$$\Psi(\vec{r},\vec{\omega}) = \chi_{\mathrm{Sun}}(\vec{r},\vec{\omega})\varepsilon(\vec{r})\exp(-\tau(\vec{r}_{\mathrm{Sun}},\vec{r})) \tag{11}$$

is used with the characteristic function of the Sun disc of diameter $\oslash_{\mathrm{Sun}}$ in radians

$$\chi_{\mathrm{Sun}}(\vec{r},\vec{\omega}) = \begin{cases} \dfrac{1}{2\pi\left(1-\cos\left(\frac{\oslash_{\mathrm{Sun}}}{2}\right)\right)} & \text{if } \vec{\omega}\cdot\dfrac{\vec{r}_{\mathrm{Sun}}-\vec{r}}{|\vec{r}_{\mathrm{Sun}}-\vec{r}|} > \cos\left(\dfrac{\oslash_{\mathrm{Sun}}}{2}\right), \\ 0 & \text{else.} \end{cases} \tag{12}$$

Atmospheric radiation can be measured e.g. by a spectrometer, which in the following is called detector. In order to formally introduce the detector, we define a detector function:

$$\varphi(\vec{r},\vec{\omega}) = \delta(\vec{r}-\vec{r}_d)\chi_{\mathrm{FOV}}(\vec{\omega}), \tag{13}$$

$$\chi_{\mathrm{FOV}}(\vec{\omega}) = \begin{cases} \Omega_{\mathrm{FOV}}^{-1} & \text{if } \vec{\omega} \in \boldsymbol{\Omega}_{\mathrm{FOV}}, \\ 0 & \text{else.} \end{cases} \tag{14}$$

Eq. (13) describes a detector at $\vec{r}_d$ with χ_{FOV} as the characteristic function of its field of view (FOV). Ω_{FOV} is the detectors FOV solid angle.

2.2. Formal solution of the integral form of the RTE

The numerical solution presented in this paper is based on the formal solution of the IRTE which can be found by applying Banachs fixed point theorem to Eq. (8) in operator form:

$$f = Kf + \Psi. \tag{15}$$

The fixed point form Eq. (15) results from introducing the operator O_{rt} with $O_{\mathrm{rt}}f := Kf + \Psi$ abbreviating the right hand side of Eq. (15). Banach's theorem allows us to construct the fixed point with $\tilde{f} = O_{\mathrm{rt}}\tilde{f}$ by successive application of O_{rt} on an initial guess, say Ψ:

$$\tilde{f} = \lim_{n\to\infty} O_{\mathrm{rt}}^n \Psi = \sum_{n=0}^{\infty} K^n \Psi \quad \text{if } \|K\| < 1. \tag{16}$$

The representation of the solution on the right side of Eq. (16) is called *Neumann series*. Prerequisite for the application of the theorem is that O_{rt} is a contraction, i.e. that O_{rt} has a Lipschitz constant smaller than one. This implies that the medium is bounded or that the single scattering albedo is smaller than 1 for a measurable subset of the medium. Information regarding the existence of a solution of the RTE for different media or for the famous Milne problem is detailed in [6,11] or [47]. Later in this paper it is shown that the summands of order n in the Neumann series are directly linked to scatter orders.

2.3. Adjoint (I)RTE and principle of reciprocity

In the context of discussing efficient numerical solutions of the RTE, the so-called *principle of reciprocity*[2] (also called *theorem of optical mutuality*) is introduced. By that principle the time direction of the radiative transfer process is reversed. In order to do this formally, a minus sign is introduced (see [6] or [11], Chapter 3 for a detailed discussion) before the direction $\vec{\omega}$ in the RTE Eq. (1), i.e. one applies the time reversal operator. This results in the so-called *adjoint RTE* containing the adjoint transport operator $k_p^\dagger[(\vec{r},\vec{\omega})\to(\vec{r}',\vec{\omega}')]$ in which $\vec{r}\leftrightarrow\vec{r}'$ and $\vec{\omega}\leftrightarrow\vec{\omega}'$ when compared to Eq. (9). The adjoint IRTE is written as

$$f^\dagger = K^\dagger f^\dagger + \varphi. \tag{17}$$

The solution of Eq. (17) is found in the same manner as for the forward time regime:

$$f^\dagger = \sum_{n=0}^{\infty} K^{\dagger n}\varphi. \tag{18}$$

By regarding the transport process in reversed time direction, sources Ψ (Sun, thermal emission) and sinks φ (detector) are exchanged. Employing the inner product $(f,g) = \int_X f(x)\, g(x)\, dx$, the theorem is expressed as follows [6]:

$$(\Psi, f^\dagger) = (f,\varphi). \tag{19}$$

[2] First formulated by Hermann von Helmholtz in "Treatise on Physiological Optics", Volume 1, 1856.

Please cite this article as: Deutschmann T, et al. The Monte Carlo atmospheric radiative transfer model McArtim: Introduction and validation of Jacobians and 3D features. JQSRT (2011), doi:10.1016/j.jqsrt.2010.12.009

Due to its mathematical relation to the detector function, in literature $f^\dagger$ is sometimes called *importance function*. Eq. (19) states that functionals of the collision density for a certain point of the phase space can be found by either determining the solution of the IRTE f and calculating (f,φ), or by determining the solution of the adjoint IRTE $f^\dagger = \sum_{n=0}^{\infty} K^{\dagger n}\varphi$ and calculating $(\Psi,f^\dagger)$. This theorem is the basis of the so-called *backward* Monte Carlo methods used to estimate RTE functionals (e.g. radiances) of small area or small FOV detectors (see also Fig. 4 later in the text).

3. Numerical solution of the RTE by Monte Carlo integration

Monte Carlo integration is particularly suitable for high dimensional integration problems. The Neumann series (Eq. (16)) is of such type. In algorithms designed to solve such integration problems, random numbers are used to draw samples from the probability density functions (PDFs) associated to the respective integration kernels. Kahn [48] showed that the most effective Monte Carlo algorithm in a computational cost sense is obtained when drawing samples from the integration kernel normalized to the integration domain and therewith transforming the kernel into a PDF on the domain. Samples of these distributions are called direct simulation samples. By drawing samples of the nested transport kernel integrals, an algorithm (ray tracing) is obtained that represents the direct simulation of the transport process.

The focus in the remainder of this paper lies on the backward Monte Carlo method which exploits the theorem of reciprocity, i.e. the trajectories start at the detector and are sampled until they are absorbed or they leave the atmosphere. In fact, the resulting ray tracing algorithm is identical to the forward Monte Carlo method, the only difference being the further treatment of the light path samples with respect to functional estimation.

3.1. Discretization of the simulation domain and input data

Prior to the ray tracing, McArtim initializes a data structure containing all atmospheric properties that are relevant to describe the RT in the domain of interest. Coordinate lists containing either plane parallel (x,y,z) or spherical radius, co-latitude and longitude coordinates define a spatial subdivision. The resulting individual cells have either plane surfaces (in the case of the plane parallel and spherical longitude grids) or curved surfaces (for radius and co-latitude grids).

In a first step, the thermodynamic and microphysical properties of the individual cells are extracted and interpolated from the input files (T, p and relative humidity), and the air density is calculated assuming air to be an ideal gas considering the pressure p and the temperature T. According to a specific wavelength, a secondary data structure with the same grid but only containing optical properties is calculated. The cells contain total extinction, absorption and scattering coefficients, the scattering coefficients of Rayleigh and rotational Raman scattering, of the individual particles, and parameters of their respective phase function. For the simulation of refraction (Snell's law) the real part of the refractive index of air is calculated according to Ciddor [49]. Additionally, the individual gaseous absorption coefficients are stored, which is not necessary for the ray tracing process but for functional evaluation.

The formula for the total extinction coefficient ε is

$$\varepsilon = \vec{n}_{\mathrm{air}}(\sigma_{\mathrm{Rayl}}+\sigma_{\mathrm{RRS}}) + \sum_{i}^{\mathrm{particles}} \varepsilon_{pi} + \sum_{i}^{\mathrm{absorbers}} n_{ai}\sigma_{ai}, \tag{20}$$

where $\vec{n}_{\mathrm{air}}$ is the number density of air. The Rayleigh cross section $\sigma_{\mathrm{Rayl}}(\lambda)$ is calculated using the numerical formula of Penndorf [50] but can also be supplemented by the user.

McArtim contains an approximate treatment of the Ring effect. The Ring effect [51,52] is commonly assumed to be caused by rotational Raman scattering (RRS, e.g. [44,53–56]). The radiance contributions attributed to RRS relative to the contribution by elastic scattering can be used to estimate the strength of the Ring effect and therewith allow us to derive information on aerosols and clouds [44]. For a derivation and details about the implemented feature see [57].

Individual particle extinction coefficients $\varepsilon_{pi}(\lambda)$ can either be provided directly by the user or can be calculated using a Mie code with an implementation following the recommendations of Wiscombe [58]. Gas number densities n_{ai} together with their absorption cross sections $\sigma_{ai}(\lambda)$ yield the gas absorption coefficients. The $\sigma_{ai}(\lambda)$ can either be defined by the user or calculated from the HITRAN database [59] according to [60, Appendix C] using p and T of the respective cell. Using the same notation as in Eq. (20), the scattering coefficient can be expressed as

$$\varepsilon_s = \vec{n}_{\mathrm{air}}(\sigma_{\mathrm{rayl}}+\sigma_{\mathrm{RRS}}) + \sum_{i}^{\mathrm{particles}} \varpi_{0i}\varepsilon_{pi}, \tag{21}$$

where $\varpi_{0i}(\lambda)$ denotes the individual particle single scattering albedo obtained from the Mie calculations or provided by the user. Particle single scattering albedos are implicitly accounted for in the total absorption coefficient and the individual scattering coefficients. The phase function parameters are accessible through pointers stored in the cells similar to the "cellular databases" described by O'Hirok and Gautier [10].

3.2. Ray tracing or trajectory sampling

An essential part of the program is a ray tracing algorithm that is described in detail in the remainder of this section. The ray tracer pursues the trajectory of a model photon through the domain by intersection point calculation and random sampling of scatter and absorption events. The ray tracing algorithm corresponds to estimating the solution of the adjoint IRTE $f^\dagger$ by drawing samples from the integrals in the Neumann series Eq. (18) using random numbers equally distributed in [0,1].

The photons originate from the detector position (hence backward Monte Carlo). The detector is described by its characteristic function like, e.g., Eq. (13) describes a detector with a circular FOV. For point like detectors with a certain FOV the initial position is $\vec{r}^*$, and the initial propagation direction $\vec{\omega}^*$ is sampled from the density $\chi_{\mathrm{FOV}}(\vec{\omega})$. When calculating radiation that propagates into

Please cite this article as: Deutschmann T, et al. The Monte Carlo atmospheric radiative transfer model McArtim: Introduction and validation of Jacobians and 3D features. JQSRT (2011), doi:10.1016/j.jqsrt.2010.12.009

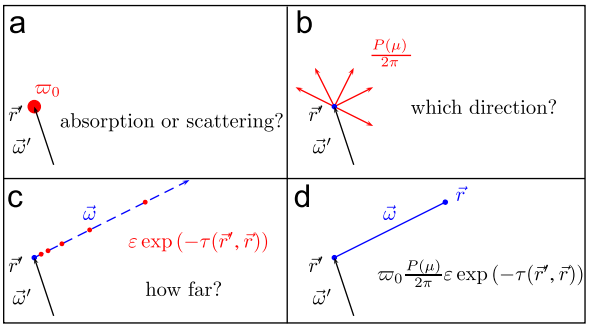

Fig. 1. Schematic depictions of the random samplings described in the Section 3.2.1 (*panel a*), 3.2.2 (*panel b*) and 3.2.3 (*panel b*). In total, the procedure generates an event $\vec{x}_{n+1}=(\vec{r},\vec{\omega})$ from its predecessor $\vec{x}_n$ represented here by $\vec{r}'$ and $\vec{\omega}'$ (*remaining panel*).

a spatially extended volume $\mathcal{R}$ of the domain (e.g. when regarding monochromatic heating rates or actinic fluxes), the initial location is sampled from the respective PDF $\chi_{\mathcal{R}}(\vec{r})$ of $\mathcal{R}$ whereas the initial propagation direction is a point sampled from the three dimensional unity sphere. Both, sampled location and direction of propagation represent the first event of the adjoint transport process $\vec{x}_0=(\vec{r}^*,\vec{\omega}^*)$ or a sample of $\varphi(\vec{r},\vec{\omega})$.

In order to sample an event $\vec{x}_{n+1}$, which corresponds to estimating $(K^\dagger)^{n+1}\varphi\approx K^\dagger\vec{x}_n$, McArtim simulates the adjoint transition density $k_p^\dagger(\vec{x}_n\to\vec{x}_{n+1})$. Because $\vec{x}_{n+1}$ only depends on the immediate predecessor $\vec{x}_n$, the resulting procedure of generating phase space samples is a Markov process. The estimation can be separated in (a) simulation of the single scattering albedo, (b) the sampling of a scatter angle from the effective phase function, and (c) sampling of the free path length (compare to Fig. 1).

3.2.1. Simulation of the single scattering albedo

Once the location of an extinction event is known, its type (absorption or scattering) is determined with a random number α_{ϖ_0}. The effective single scattering albedo ϖ_0 is the ratio of the total scatter coefficient ε_s defined in Eq. (21) and the total extinction coefficient ε in Eq. (20). Using α_{ϖ_0}, ϖ_0 is simulated by testing $\alpha_{\varpi_0}>\varpi_0$. If this condition is met, the photon is absorbed. Otherwise scattering occurs. This approach is also referred to as *Russian roulette technique*. If the photon is scattered, i.e. if it survives the Russian roulette, the trajectory sampling procedure is continued as described in the next Section 3.2.2. Otherwise the trajectory is terminated and the (adjoint) collision density estimate is complete.

3.2.2. Sampling of the scatter angle

The effective phase function is denoted by

$$P(\mu)=\varepsilon_s^{-1}\sum_i^{\text{particles}}\varpi_{0i}\varepsilon_{pi}P_i(\mu), \tag{22}$$

where the ϖ_{0i} are set to one for Rayleigh and RRS scattering. The anisotropic Rayleigh phase function $P_{\text{Rayl}}(\mu)=y_+ + y_-\mu^2$ (see [61]) is defined by

$$y_\pm=\frac{3(1\pm\rho(\lambda))}{2(2+\rho(\lambda))}\quad\text{with }\rho(\lambda)=6\frac{F_\lambda-1}{2+7F_\lambda}. \tag{23}$$

The King correction factor is $F_\lambda=1.0367+5.381\times10^{-16}\lambda^{-2}+0.304\times10^{-28}\lambda^{-4}$ according to [62]. The RRS phase function is defined as

$$P_{\text{RRS}}(\mu)=\tfrac{3}{40}(13+\mu^2). \tag{24}$$

The selection of random scatter angles consists of two steps. First, the selection of the scatter object and, then, sampling a scatter angle according to the particular phase function. For the former, a random number α_o is drawn. The index of the scatter object o is determined according to the relation

$$o=\min_o\left\{\sum_i^o\varepsilon_{pi}>\alpha_o\varepsilon_s\right\}. \tag{25}$$

Depending on the phase function $P_o(\mu)$ a new propagation direction is chosen. The azimuth angle φ is found by $\varphi=2\pi\alpha_\varphi$ and μ is selected by applying the inverse cumulative distribution function of the phase function to a random number $2\alpha_\mu$.

In the case of Rayleigh and RRS scattering, Cardan's formulas are used, whereas for aerosol and cloud particles several different models (Henyey–Greenstein, Legendre polynomial expansion, table methods) have been implemented.

3.2.3. Free path length sampling

The remaining step in the procedure of sampling the event $\vec{x}_{n+1}$ from $\vec{x}_n$ is to determine the photon's free path length (FPL) with the CDF $P_l(\vec{r})$

$$P_l(\vec{r})=\exp(-\tau(\vec{r}_n,\vec{r}_{n+1})), \tag{26}$$

where ε_i refers to the total extinction coefficient in an individual cell. The indices (i and l in the following) begin with the cell corresponding to $\vec{r}_n$.

According to the chosen discretization of the atmosphere, the polygon between $\vec{r}_n$ and $\vec{r}_{n+1}$ is subdivided into l segments of length d_i, each with constant extinction coefficients ε_i (see Fig. 2). At each polygon point refraction is simulated using Snell's law according to the cell refractive indices. To sample $\vec{r}_{n+1}$ from Eq. (26) a random number α_l is drawn and a corresponding optical thickness is calculated:

$$\tau_l=-\ln(\alpha_l). \tag{27}$$

By gradually summing up the τ_i, the cell index l of $\vec{r}_{n+1}$ can be determined:

$$l=\max_{l=1,\dots}\left\{\sum_{i=1}^l d_i\varepsilon_i<\tau_l\right\}. \tag{28}$$

In order to find the exact position of $\vec{r}_{n+1}$ in the cell l, the distance d_l between $\vec{r}_{n+1}$ and the last intersection point between the LOS and the cell boundary is calculated:

$$d_l=\frac{\tau_l-\sum_{i=1}^{l-1}d_i\varepsilon_i}{\varepsilon_l}. \tag{29}$$

In the case that the sampled optical thickness exceeds the optical thickness through the atmosphere along the propagation direction, the photon escapes from the atmosphere and the trajectory is terminated at the location of the last scatter event.

Please cite this article as: Deutschmann T, et al. The Monte Carlo atmospheric radiative transfer model McArtim: Introduction and validation of Jacobians and 3D features. JQSRT (2011), doi:10.1016/j.jqsrt.2010.12.009

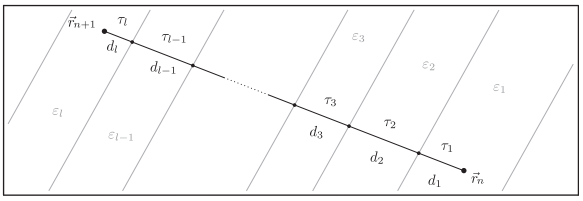

Fig. 2. Estimation of the free photon path length $|\vec{r}_{n+1}-\vec{r}_n|$ (schematic in Fig. 1, panel 1). The ray tracer subdivides the medium into τ−segments according to the spatial grid and determines $\vec{r}_{n+1}$ by sampling of the optical density τ_l between $\vec{r}_n$ and $\vec{r}_{n+1}$.

3.2.3.1. Ray tracing on spherical 3D grids. At presence there are four grid types implemented: plane parallel 1D/3D and spherical 1D/3D grids. In the remainder of this section on FPL sampling, we want to describe a, to our knowledge, unique feature of McArtim: ray tracing on spherical 3D (sp3D) grids. During the ray tracing McArtim updates two closely related quantities: the position of the model photon $\vec{p}$ in the atmosphere and the 3D grid indices $(i_{x|\varphi},i_{y|\theta},i_{z|r})$ of $\vec{p}$ relative to the respective grid. The problem of finding the intersection point of the model photon at $\vec{p}$ propagating into direction $\vec{k}$ with the boundary of the sp3D grid cell states:

$$\begin{pmatrix} p_x+\lambda k_x \\ p_y+\lambda k_y \\ p_z+\lambda k_z \end{pmatrix} = \begin{pmatrix} r_{A|B}\cos\varphi_{A|B}\sin\theta_{A|B} \\ r_{A|B}\sin\varphi_{A|B}\sin\theta_{A|B} \\ r_{A|B}\cos\theta_{A|B} \end{pmatrix}. \tag{30}$$

The spherical coordinates indexed with A and B mark the adjacent grid coordinates of the cell. Due to the structure of the solution for λ it is advantageous to know in advance, whether an intersection point with the respective A or B surface can be expected. This is examined by calculating the scalar product of $\vec{k}$ with the spherical unit vectors $\vec{e}_r$, $\vec{e}_\theta$ and $\vec{e}_\varphi$ at $\vec{p}$. The sign of the product tells us whether to test for intersection with the surface lying into positive (B) or negative (A) direction along the grid.

The distance to the cell boundary is calculated employing the following formulas:

- Radius surfaces $r=const$. The surfaces are spheres and the resulting equation for λ is quadratic:

$$\sum_{i=x,y,z}(p_i+\lambda k_i)^2=r_{A|B}^2 \Rightarrow \lambda^2+2\lambda\sum_{i=x,y,z}p_i k_i+\sum_{i=x,y,z}p_i^2-r_{A|B}^2=0. \tag{31}$$

- Co-latitude surfaces $\theta=const$. The surfaces are cones oriented along the $\vec{e}_z$ axis with the half aperture angle $\theta_{A|B}$ obeying the equation:

$$\vec{e}_z\frac{\vec{r}}{|\vec{r}|}=\cos(\theta_{A|B}) \Rightarrow x^2+y^2-\tan^2(\theta_{A|B})z^2=0. \tag{32}$$

  Inserting Eq. (30) into Eq. (32) yields quadratic equations in λ.
- Longitude surfaces $\varphi=const$. These surfaces are planes. The condition for the inter section point can be derived from the ratio of the first two coordinates of Eq. (30):

$$\tan\varphi_{A|B}=\frac{p_y+\lambda k_y}{p_x+\lambda k_x} \Rightarrow \lambda=\frac{p_y-p_x\tan\varphi_{A|B}}{k_x\tan\varphi_{A|B}-k_y}. \tag{33}$$

The most famous problem with ray tracing on spherical grids occurs, when $\vec{p}$ is located on a cell boundary and the inter section is searched with the same cell boundary. This can happen when the grid index $(i_{x|\varphi},i_{y|\theta},i_{z|r})$ is determined from $\vec{p}$. Due to the limited machine precision the index will flicker between two adjacent cells. If the "wrong" index is chosen the solution for λ as a result of the formulas above will be in the range of the machine precision, and the ray tracing algorithm enters an infinite loop. Our experience has shown that it is worthwhile to accept the finite machine precision and declare the photon to be forward propagated to the adjacent cell and thereby to update the grid index.

3.2.4. Ground scattering

During the FPL ray tracing procedure, the ray occasionally intersects the Earth's surface. In this case, McArtim samples the type of interaction (absorption or scattering) using the respective surface albedo and samples a new propagation direction according to the properties of a Lambertian reflector, i.e. the cosine of the scattering angle relative to the local surface normal μ_L is sampled by

$$\mu_L=\sqrt{\alpha} \tag{34}$$

using a random number $\alpha\in[0,1]$.

Besides the simple plane parallel resp. curved surface of the spherical grids a more detailed description of the surface topography is implemented. The x_i/y_j, respectively, φ_i/θ_j grids define a horizontal sub division of the surface into 2D cells. For each point of the joint grid (x_i/y_j) an altitude value h_{ij} can be defined yielding a point $\vec{r}(x_i,y_j,h_0+h_{ij})$ where h_0 marks the neutral elevation of the ground, i.e. the Earth radius in case of the spherical grids. The function $\vec{r}$ maps the grid coordinates to the absolute position. Using the four corner altitudes a fifth point $\vec{m}_{ij}$ is calculated as follows:

$$\vec{m}_{ij}=\vec{r}(\tfrac{1}{2}(x_i+x_{i+1}),\tfrac{1}{2}(y_j+y_{j+1}), h_0+\tfrac{1}{4}(h_{ij}+h_{i+1j}+h_{ij+1}+h_{i+1j+1}). \tag{35}$$

These five points define four triangles with the same corner at $\vec{m}_{ij}$ forming a surface description in the 2D grid cell ij. We believe that the feature is implemented correctly. However, a validation is necessary. A similar approach of modeling topography has recently been presented in Mayer et al. [63].

3.2.5. Escape from the atmosphere or absorption

The sampling procedure described in Sections 3.2.1, 3.2.2, 3.2.3 and 3.2.4 is repeated until an absorption event occurs, or until the photon leaves the atmosphere. The trajectory (or event chain) $\vec{x}_0,\vec{x}_1,\ldots,\vec{x}_n$ can then be regarded as a sample of the adjoint collision density $f^\dagger(\vec{x}^*)$. Fig. 3 shows three example depictions of events resulting from the detailed backward Monte Carlo algorithm applied to a model atmosphere described in Section 5.3.

Please cite this article as: Deutschmann T, et al. The Monte Carlo atmospheric radiative transfer model McArtim: Introduction and validation of Jacobians and 3D features. JQSRT (2011), doi:10.1016/j.jqsrt.2010.12.009

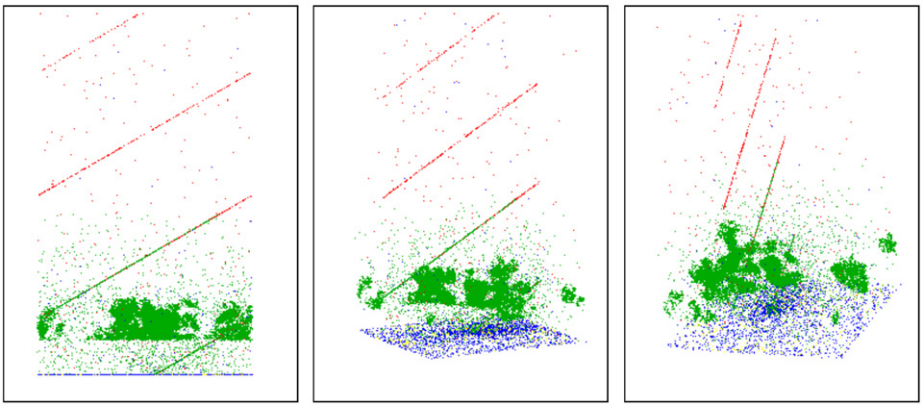

Fig. 3. Backward trajectory events occurring when observing $\lambda = 670$ nm radiation scattered at a cumulus (Cu) cloud (see Section 5.3 and the Figs. 8 and 9 for the resulting radiance fields). Three perspectives of the simulated domain (base size 6.67×6.67 km^2) are shown. Green points represent cloud and aerosol particle scatter events, blue points depict absorption events. Ground scattering is shown in yellow and red dots symbolize Rayleigh scattering by air molecules. The Rayleigh scatter events located on the periodically continued (periodic boundary conditions) line of sight are the first events occurring when the photon ray enters the atmosphere. According to the optical properties, the following scatter events "in line" are those by aerosol and cloud particles. Notice that the optical properties of the whole domain contribute to functionals (see Section 4) calculated from this ensemble of photon trajectories.

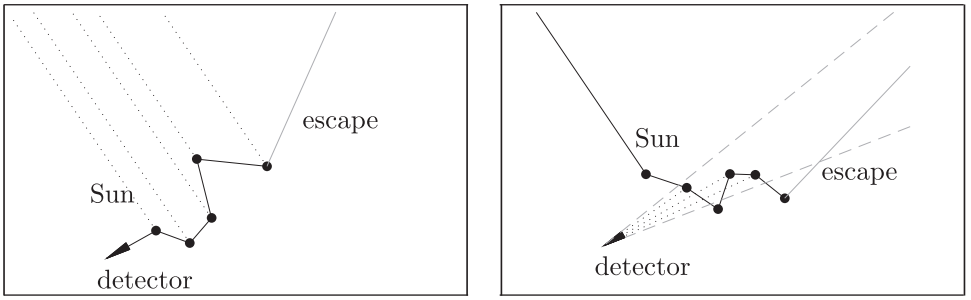

Fig. 4. *Left panel*: Backward photon trajectory ($f^\dagger$ estimate, solid polygon line) originating from the detector. *Right panel*: Forward photon trajectory (f estimate, solid polygon line) originating from the Sun. In the forward approach only scatter events $\vec{r}_i$ (dots) inside the FOV (dashed gray lines) contribute (dotted lines) to a simulated measurement, whereas every scatter event yields a contribution (dotted lines) when exploiting a backward trajectory sample of $f^\dagger$.

4. Calculated physical quantities

A Monte Carlo trajectory is a physically representative sample of a light path. At the same time it is an estimate of the integrals in the Neumann series (see Eq. (16) or Eq. (18)). Several measurable quantities such as radiances, light path integrals (obtainable e.g. by means of spectroscopy) and their Jacobians with respect to optical atmospheric parameters can be expressed as functionals of the collision densities f (respectively, $f^\dagger$ using the adjoint RT theory). Fig. 4 shows two estimates of f and $f^\dagger$, respectively.

In literature, the related formulas are known as local estimates and dependent sampling [6,11]. In order to facilitate the readability, the following notation is introduced:

$$\mu_n^* \coloneqq \frac{\vec{r}_{\text{Sun}} - \vec{r}_n}{|\vec{r}_{\text{Sun}} - \vec{r}_n|} \cdot \vec{\omega}_{n-1}, \tag{36}$$

$$\mu_{i,j} \coloneqq \vec{\omega}_i \cdot \vec{\omega}_j, \tag{37}$$

$$[ab](\vec{r}) \coloneqq a(\vec{r})b(\vec{r}) \quad \text{and} \quad [ab]_c \coloneqq a_c b_c, \tag{38}$$

$$s_n(\mu) \coloneqq \sum_{t=1}^{N_s} [\varpi_{0,t}\varepsilon_t P_t(\mu)](\vec{r}_n), \tag{39}$$

$$\tau_{*\to n\to\cdots\to 0} \coloneqq \tau(\vec{r}_{\text{Sun}}, \vec{r}_n) + \sum_{i=1}^{n} \tau(\vec{r}_{i-1}, \vec{r}_i). \tag{40}$$

The μs in Eq. (36), (37) and (39) are cosines of scatter angles, N_s is the number of scatterers in the cell corresponding to $\vec{r}_n$. Eq. (38) is needed only to avoid repeated indexing of quantities associated to individual cells. The $s_n(\mu)$ in Eq. (39) can be interpreted as an optical density of a scatter event involving a certain ϖ_0 and a phase function $P(\mu)$. Eq. (40) is an abbreviation for the optical thickness between the Sun and the detector through a photon trajectory with n scatter events.

In the following, formulas for estimates y_n of functionals y will be given. Such an estimate y_n can be obtained from a single trajectory generated by the algorithm described in the previous section. In order to calculate a functional with a certain accuracy the estimates y_n obtained from a sufficiently large number of trajectories N have to be

Please cite this article as: Deutschmann T, et al. The Monte Carlo atmospheric radiative transfer model McArtim: Introduction and validation of Jacobians and 3D features. JQSRT (2011), doi:10.1016/j.jqsrt.2010.12.009

averaged:

$$\langle y\rangle \approx \frac{1}{N}\sum_{n=1}^{N} y_n. \tag{41}$$

The variance of a functional is obtained by

$$\sigma^2(y) \approx \frac{1}{N}\sum_{n=1}^{N} y_n^2 - \left(\frac{1}{N}\sum_{n=1}^{N} y_n\right)^2. \tag{42}$$

The convergence of the means towards the true value of the functionals with increasing N relies on the law of large numbers.

4.1. Radiances

One basic functional of interest is the radiance I_* which is given by

$$I_*(\vec{r}^*,\mathbf{\Omega}_{\mathrm{FOV}}) = \frac{1}{\varepsilon(\vec{r}^*)}\int_{\mathbf{\Omega}_{\mathrm{FOV}}} f(\vec{r}^*,\vec{\omega})\, d\vec{\omega} = \frac{1}{\varepsilon}(f,\varphi), \tag{43}$$

where the inner product of f and Eq. (13) is used. The radiance is a quantity that is closely related to the collision density. I_* is calculated by integrating the collision density over the spatial directions of the field of view and subsequent normalization with the extinction coefficient. I_* can be obtained either from a forward trajectory ensemble as in Eq. (43), or from a backward trajectory ensemble exploiting the principle of reciprocity:

$$I_* = \frac{1}{\varepsilon}(f,\varphi) = \frac{1}{\varepsilon}(\Psi,f^\dagger) = \frac{1}{\varepsilon}\sum_{n=0}^{\infty}(\Psi,K^{\dagger n}\varphi). \tag{44}$$

For a single backward trajectory with N scatter events, an estimate of I_* is calculated by carrying out the integrals in Eq. (18):

$$I_* \approx \sum_{n=0}^{N} c(\vec{r}_n) w_n, \tag{45}$$

with

$$w_n = e^{-\tau_{*\to n}} P(\vec{r}_n,\mu_n^*). \tag{46}$$

The trajectory is an estimate for $f^{(\dagger)}$ such that the integrals in Eq. (18) assume the simple form Eq. (45). The function $c(\vec{r}_n)$ approximately equals the solid angle area of the Sun disc as seen from $\vec{r}_n$. Due to the large distance between Earth and Sun, $c(\vec{r}_n)$ can be regarded as constant and is therefore omitted in the derivations that follow. The weight w_n can be interpreted as the joint probability for the transmission of light over the distance between the Sun and the point $\vec{r}_n$, and the probability of scattering with the cosine of the scatter angle μ_n. In the current implementation of McArtim refraction is not taken into account in the trajectory part between the Sun and the particular scattering event of the local estimate.

In the next section, Jacobians of the radiance with respect to optical parameters of the atmosphere are considered. Actinic fluxes (AF) can be obtained by assuming the detector's FOV is 4π. The only difference to Eq. (45) is that the direct light contribution is also accounted for. Therefore, the following discussion on radiance Jacobians also addresses Jacobians of AFs.

4.2. Jacobians of the radiance

In order to reconstruct the state of the atmosphere from a spectroscopic measurement of scattered Sun light, Jacobians of the measured quantities with respect to parameters of the RT are needed for certain cells (in the following indexed with c). In the context of inversion the state could for example be the number density profile of a trace gas or the extinction coefficient profile of an aerosol. Thus, the state components ξ of interest are usually the absorption coefficient β_c as well as optical aerosol properties e.g. extinction coefficient ε_c, single scattering albedo $\varpi_{0,c}$ or phase function parameters as for instance the asymmetry parameter g for the Henyey–Greenstein model or Legendre polynomial coefficients for more complicated phase functions.

Formulas for estimates of radiance Jacobians were first calculated by Marchuk et al. [6]. In order to calculate these quantities, McArtim uses *importance sampling* (sometimes also referred to as *dependent sampling*). The idea behind this technique is to approximate a complicated kernel by a kernel whose cumulative distribution function (CDF) is analytically invertible. The samples are then drawn from the simple PDF and each sample is weighted with the ratio of the true PDF and its approximation. Importance sampling is necessary in the context of atmospheric Monte Carlo RTM because direct sampling of Jacobians involves complicated integration kernels and non-analytic CDFs which would require large computational efforts for their inversion. Another advantage of the technique is that one trajectory ensemble can be used to estimate all derivatives simultaneously. The drawback, however, is a large variance of the estimates.

The fundamental term for the calculation of Jacobians is

$$\Gamma_n = -\tau_{*\to n\to 0} + \ln(s_n(\mu_n^*)) + \sum_{i=1}^{n-1}\ln(s_i(\mu_{i,i-1})). \tag{47}$$

Γ_n can be derived from the logarithm of the kernel in the nth summand of the Neumann series (see [6] for details). Eq. (47) can be interpreted as the optical thickness along the light path considering scattering processes. Using Eq. (47) the structure of the estimate of a Jacobian is

$$\frac{d}{d\xi}I_* \approx \sum_{n=0}^{N} w_n \frac{d}{d\xi}\Gamma_n. \tag{48}$$

4.2.1. Absorption coefficient Jacobians

The simplest expression of a Jacobian is obtained for derivatives with respect to the absorption coefficient $\xi = \beta_c$:

$$\frac{d}{d\beta_c}\Gamma_n = -l_c^n, \tag{49}$$

where l_c^n is the path length of the trajectory n (with n scatter events) in the cell c. In order to obtain absorption coefficient Jacobians of the radiance Eq. (49) is inserted into Eq. (48). For a certain absorber, β_c is the product of the wavelength dependent absorption cross section $\sigma_c(\lambda)$ and the number density n_c. After applying the chain rule, the number density Jacobians are given by

$$\frac{d}{dn_c}I_* = \sigma_c(\lambda)\frac{d}{d\beta_c}I_*. \tag{50}$$

Please cite this article as: Deutschmann T, et al. The Monte Carlo atmospheric radiative transfer model McArtim: Introduction and validation of Jacobians and 3D features. JQSRT (2011), doi:10.1016/j.jqsrt.2010.12.009

For later purposes we introduce the intensity weighted photon path length L_c through the cell c:

$$L_c = -\frac{d}{d\beta_c}\ln(I_*) = \frac{\left\langle \sum_n^N w_n l_c^n \right\rangle}{\left\langle \sum_n^N w_n \right\rangle}. \tag{51}$$

In order to evaluate DOAS slant column density measurements, the box air mass factor of the box c with the height h_c is defined as

$$\mathrm{BoxAMF}_c = \frac{L_c}{h_c}. \tag{52}$$

The BoxAMF can be interpreted as the ratio of the intensity weighted light path length in the cell c and the box height h_c.

4.2.2. Jacobians of optical particle properties

The relevant optical properties of a particle t in the cell c are the extinction coefficient ε_{ct}, the single scattering albedo $\varpi_{0,ct}$ and phase function parameters such as the asymmetry parameter g_c or higher Legendre moments. The calculation of the respective derivatives from Eq. (47) results into:

$$\frac{d}{d\varepsilon_{ct}}\Gamma_n = -l_c^n + \sum_{i=1}^{n-1}\frac{\chi_c(\vec{r}_i)}{s_i(\mu_{i,i-1})}[\varpi_{0,t}P_t(\mu_{i,i-1})]_c(\vec{r}_i) + \frac{\chi_c(\vec{r}_n)}{s_n(\mu_n^*)}[\varpi_{0,t}P_t(\mu_n^*)]_c, \tag{53}$$

$$\frac{d}{d\varpi_{0,ct}}\Gamma_n = \sum_{i=1}^{n-1}\frac{\chi_c(\vec{r}_i)}{s_i(\mu_{i,i-1})}[\varepsilon_t P_t(\mu_{i,i-1})]_c + \frac{\chi_c(\vec{r}_n)}{s_n(\mu_n^*)}[\varepsilon_t P_t(\mu_n^*)]_c, \tag{54}$$

$$\frac{d}{dg_c}\Gamma_n = \sum_{i=1}^{n-1}\frac{\chi_c(\vec{r}_i)}{s_i(\mu_{i,i-1})}\left[\varpi_{0,t}\varepsilon_t\frac{\partial P_t(\mu_{i,i-1})}{\partial g}\right]_c + \frac{\chi_c(\vec{r}_n)}{s_n(\mu_n^*)}\left[\varpi_{0,t}\varepsilon_t\frac{\partial P_t(\mu_n^*)}{\partial g}\right]_c, \tag{55}$$

where $\chi_c(\vec{r})$ is a characteristic function of the cell c that assures that only scatter events located at $\vec{r}$ inside the cell c contribute to the sum. In comparison to Eq. (49), the structure of Eq. (53) contains an additional expression that originates from the derivative of the effective phase function. The l_c^n is missing in Eq. (54) because the optical density along the trajectory does not depend on $\varpi_{0,ct}$. In Eq. (55), the asymmetry parameter can formally be exchanged by any other phase function parameter, e.g. higher moments of Legendre polynomials.

4.3. Light path integrals

Certain spectroscopic analysis techniques yield light path integrals (LPIs) of gas number densities (e.g. slant column densities (SCDs) from DOAS), water (liquid water path: LWP) or ice content (ice water path: IWP). McArtim calculates these quantities using logarithmic derivatives of the radiance with respect to the absorption coefficient L_c in all cells of the domain grid. Using all L_c, the LPI of a physical property with the density $n(\vec{r})$, respectively, n_c in the cell c is given by

$$\int_{\text{light path}} n(\vec{r})\,dr \approx \sum_c^{\text{cells}} L_c n_c. \tag{56}$$

Eq. (56) is only an approximation with regard to the discretization of the atmosphere into cells, each containing a constant number density n_c.

4.3.1. Jacobians of light path integrals

The last type of Jacobians discussed in this section are those of LPIs defined in Eq. (56). These Jacobians are particularly interesting when applying the O_4 method (e.g. [30–32]) for aerosol property retrievals, or for interpreting spectroscopic measurements with respect to ice and liquid water paths. McArtim uses Jacobians of the L_c to calculate LPI Jacobians:

$$\frac{d}{d\xi}L_c = -\frac{d}{d\xi}\frac{d}{d\beta_c}\ln(I_*) \tag{57}$$

$$\frac{d}{d\xi}L_c = -\frac{I_*\dfrac{\partial^2 I_*}{\partial\xi\partial\beta_c} - \left(\dfrac{dI_*}{d\beta_c}\right)\left(\dfrac{dI_*}{d\xi}\right)}{I_*^2} \tag{58}$$

$$\frac{d}{d\xi}L_c = L_c X_\xi - Y_{c\xi}. \tag{59}$$

Here, X_ξ is the logarithmic derivative of the radiance I_* with respect to ξ. $Y_{c\xi}$ is a "mixed" derivative containing the intensity weighted derivatives of I_* with respect to β_c and ξ. L_c and X_ξ are calculated in the manner described in Section 4.2.2. In order to calculate $Y_{c\xi}$, the respective logarithmic derivatives of a single intensity estimate are multiplied for each scatter event n and weighted by w_n.

4.3.2. Effective number of scatter events of one type

The effective number of scatter events of one type is obtained by calculating the intensity weighted scatter count of the respective optical constituent p:

$$N_p = \frac{\left\langle \sum_{n=0}^{\infty} N_{p,n} w_n \right\rangle}{\left\langle \sum_{n=0}^{\infty} w_n \right\rangle}. \tag{60}$$

Here, $N_{p,n}$ denotes the number of scatter events on particles of the type p on a trajectory sample of order n. In Section 5.3.1 these quantities are used to demonstrate how clouds influence the scatter processes at the ground by air molecules and aerosol particles.

5. McArtim features, inter comparison and validation

The primary radiation quantities calculated by McArtim are radiances, actinic fluxes, (monochromatic) heating rates and Jacobians of these quantities with respect to (3D) cellular optical properties such as the absorption coefficient, and the optical particle properties extinction coefficient, single scattering albedo and phase function parameters. Additionally, McArtim calculates effective numbers of scatter events for molecular, ground and particle scattering and radiance contributions attributed to photons interacting with the ground, as well as photon path length distributions.

Particle optical properties can be defined directly, where the Henyey–Greenstein model or an expansion into

Please cite this article as: Deutschmann T, et al. The Monte Carlo atmospheric radiative transfer model McArtim: Introduction and validation of Jacobians and 3D features. JQSRT (2011), doi:10.1016/j.jqsrt.2010.12.009

Legendre polynomials is employed to parametrize the scattering phase functions. For certain purposes (materials) Rayleigh phase functions can also be selected. Alternatively, particle optical properties can be defined indirectly by defining microphysical parameters such as 3D fields of N log normal size distributions, or size bins, and a wavelength dependent complex refractive index. Internally, a Mie code is used to map microphysical to optical parameters.

Gaseous absorption can be quantified by 1D/3D number density distribution profiles and location dependent absorption cross sections. For some gases, the HITRAN database can be utilized, the program then internally calculates pressure and temperature dependent cross sections using the HITRAN data for each cell of the chosen grid.

The supported grids are spherical 1D/3D and plane parallel 1D/3D. For all grid types a heterogeneous multispectral ground albedo map can be defined, whereas for the 3D grids topographic surface information can also be included into the model.

In previous radiative transfer model inter comparisons, only radiances and box air mass factors were validated [15]. Regarding these quantities, McArtim was intensively compared with TRACY-II and an agreement was found within the Monte Carlo noise range. Although the McArtim code originates from the code of TRACY-II, several aspects are fundamentally different. For instance in TRACY-II gaseous, particle or surface absorption is not accounted for during the path generation but it is considered during the subsequent functional calculation by applying the equivalence theorem. The separation of absorption and scattering allows modification of the absorbing components using a single trajectory ensemble without increasing the variance of the estimated functionals. However, the drawback of this procedure is its high computational costs since the transmittance has to be calculated for each trajectory of the ensemble. This involves summations of optical thickness snippets along the sampled paths followed by the invocation of an exponential function in each scatter order. In addition, the functionals may contain many small contributions originating, for instance, from scatter events after a ground scatter event in the chain. Therefore, TRACY-II is much slower than McArtim especially for small ground albedo and clouds.

In the following, comparisons of measured and modeled radiances are shown. Further, since McArtim also provides new functionals and Jacobians, these quantities are validated by self-consistency tests. The 3D features of McArtim have partially been investigated by [64,65]. The section is therefore concluded with inter comparison exercises for some scenarios of the I3RC [37].

5.1. Comparison to measurements

The most direct method to validate a RTM is clearly to compare its results to measurements. However, a limitation of this approach arises from the uncertainty of the atmospheric state during such a measurement which is often too large to support a precise simulation of the measurements using the RTM. One region of the atmosphere in which the state is fairly well constrained is the stratosphere. There, RT is predominantly determined by Rayleigh scattering by air molecules and absorption by ozone in the UV spectral range. For all model calculations shown in this sub section, a standard atmosphere excluding aerosol or cloud particles is used.

Here, the radiances modeled by McArtim are compared to those measured by the balloon-borne limb scanning mini-DOAS instrument deployed during the StraPolÉte campaign in September 2009. The campaign took place at the Esrange Space Center located near Kiruna (67.9°N, 22.1°E) in northern Sweden. During the campaign the mini-DOAS instrument [24] consisting of two optical spectrometers, an Ocean Optics USB2000 with FWHM ≈ 0.7 nm (6.2 pixels) and a QE65000 with FWHM ≈ 0.4 nm (4.75 pixels) was mounted on the LPMA/DOAS payload and launched into the stratosphere on September 7th 2009 at 14.50 UT. After two hours of ascent (at around 16:45 UT) the float altitude was reached at 32 km. The balloon stayed on float while limb scanning measurements were performed during sunset and sunrise on September 8th 2009. During all measurements the relative solar azimuth angle was kept constant at 90°.

Fig. 5 inter compares measured and modeled radiances for the wavelengths 350, 370 and 390 nm (from the QE65000) and 420, 465 and 490 nm (from the USB2000) for the balloon ascent for which the telescope elevation was fixed to 0°. The measured radiances are routinely corrected for the detector dark current and offset, and are averaged over 5 adjacent spectrometer channels (i.e. 5 channels roughly correspond to a 1 nm range around the center wavelength). In order to be able to compare the uncalibrated measured fluxes to the modeled fluxes, both are normalized to the radiances obtained at the float position.

Aiming at investigating the performance of McArtim for high SZAs, Fig. 6 inter compares measured and modeled radiances as a function of the SZA at the float altitude over Kiruna during sunrise. The same normalization procedure as described for Fig. 5 is applied to the measured and modeled radiances. In this figure only radiances of the visible spectral range are shown due to a technical problem with the UV spectrograph.

With increasing altitude, the recorded light is less affected by multiple scattering processes. Additionally, the sampled atmosphere becomes optically thinner due to the fading presence of aerosol and cloud particles, and molecular scattering becomes the dominating scatter process. Therefore, and also due to the chosen normalization method, the uncertainties decrease with altitude. During the ascent above 10 km, the balloon gondola suffered from pendulum oscillations causing perturbations of the viewing direction and, thereby, perturbations of the measured radiances. Since these movements are not recorded by any inertial state measuring device, they are not accounted for by the model. Another RT uncertainty is the spectral ground albedo for the measurement site. In the model settings a gray (wavelength independent) albedo of 0.05 is assumed. Uncertainties in the aerosol load can be reduced by performing a detailed inversion of the aerosol optical properties. In this study, however, a purely Rayleigh scattering atmosphere was assumed not containing any particles.

Please cite this article as: Deutschmann T, et al. The Monte Carlo atmospheric radiative transfer model McArtim: Introduction and validation of Jacobians and 3D features. JQSRT (2011), doi:10.1016/j.jqsrt.2010.12.009

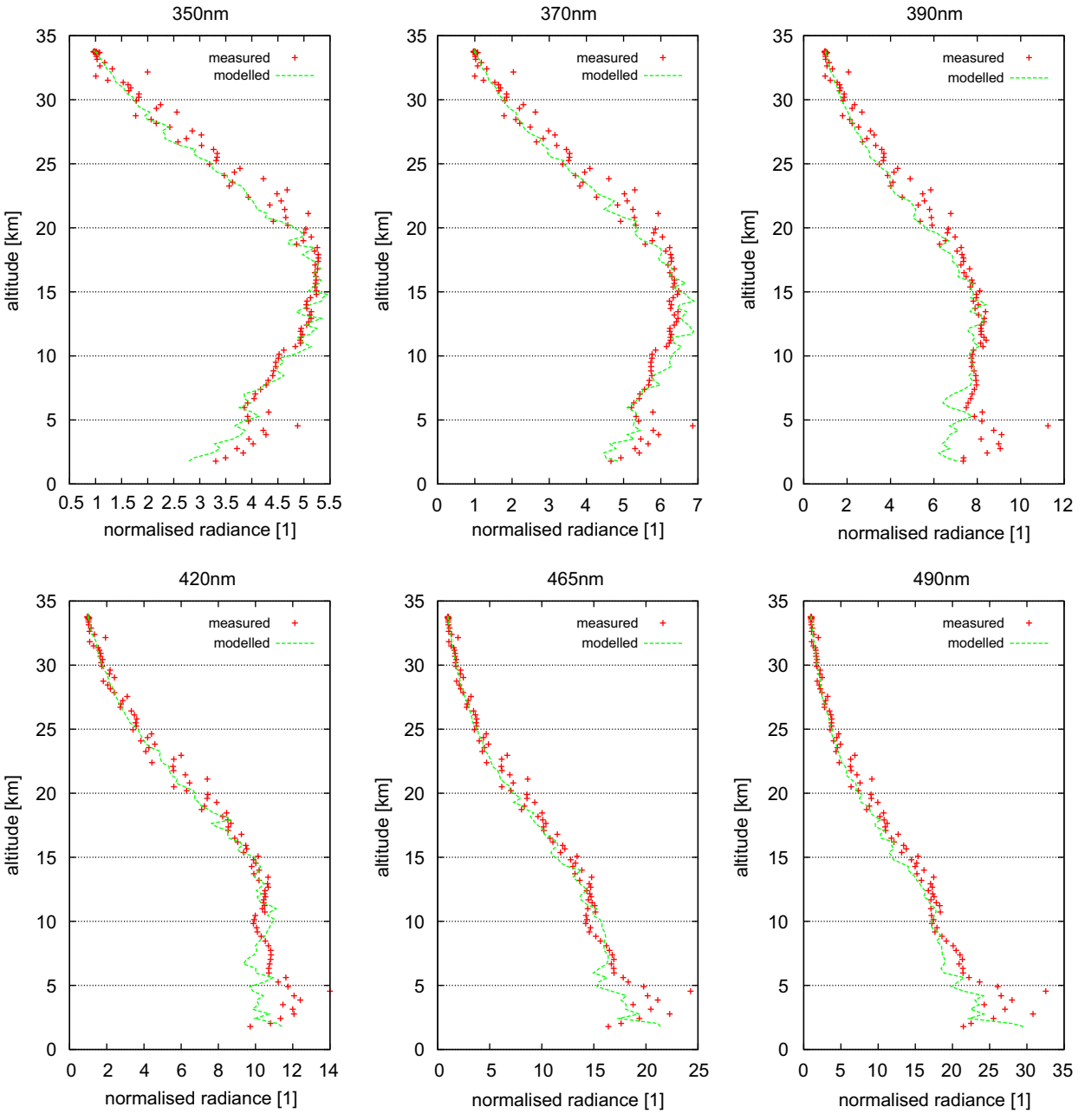

Fig. 5. Comparison of measured (red crosses) and modeled (green dashed lines) normalized radiances for different wavelengths during the balloon gondola ascent of the mini DOAS over Kiruna, Sweden on September 7th 2009, between 14:53 (lift off) and 17:01 when reaching the float position. Using trajectory data with a time resolution of 1 Hz, the modeled radiances were obtained by averaging, thus simulating time integration by the spectrometers. The radiance normalization was achieved by dividing by radiances obtained in the float position (see text for details). *Top panel*: QE65000 and *bottom panel*: USB2000 optical. (For interpretation of the references to color in this figure legend, the reader is referred to the web version of this article.)

Possible reasons for the deviations observed between model and measurement at large SZA are:

- *Polarization effects*: As already mentioned in Section 2, in the measurement geometry under consideration deviations of the "scalar" radiance can be expected due to polarizing effects of the prevailing molecular Rayleigh scattering.
- Refraction affecting the light path between a scatter event and the Sun since currently refraction is not simulated for these parts of the photon trajectories.
- The so-called center-to-limb-darkening (CLD) effect [66]. This effect originates from different Fraunhofer spectra at the center compared to those at the edge of the Sun disc in combination with a strong transmission gradient over the Sun disc in the limb measuring geometry at large SZA.

Please cite this article as: Deutschmann T, et al. The Monte Carlo atmospheric radiative transfer model McArtim: Introduction and validation of Jacobians and 3D features. JQSRT (2011), doi:10.1016/j.jqsrt.2010.12.009

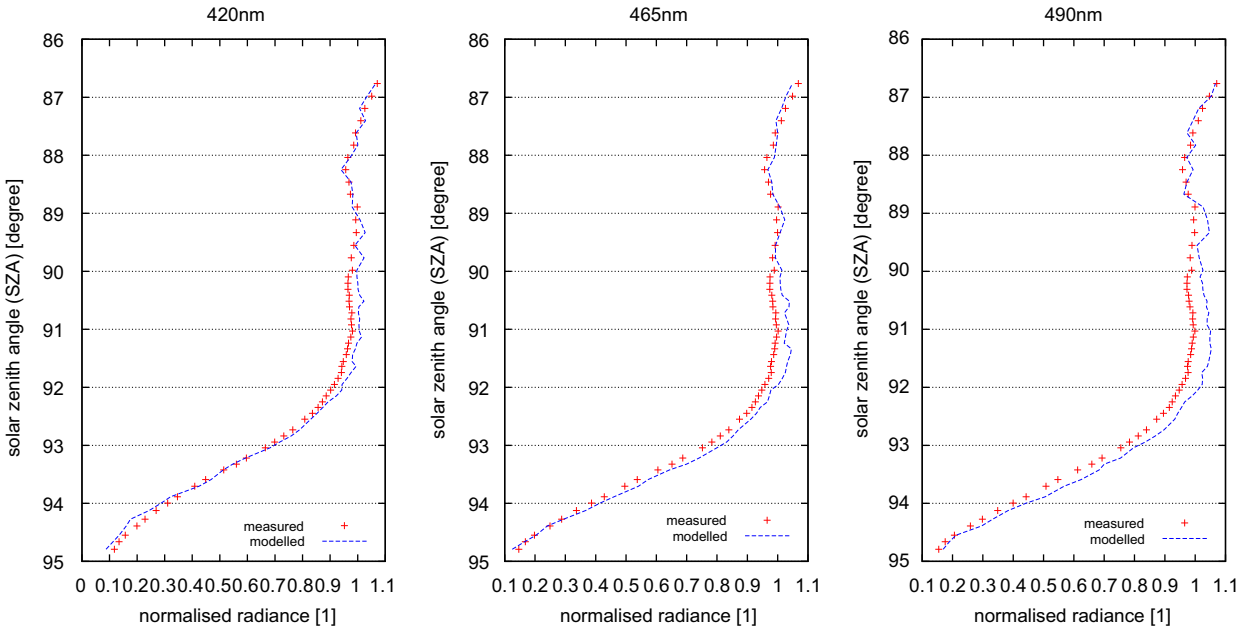

Fig. 6. Comparison of modeled and measured radiances during sunrise at the float position over Kiruna (for details see text).

- 3D uncertainties in the atmospheric property and surface composition at the tangent point, i.e. where the local SZA is exactly 90°. By varying the vertical aerosol extinction profile and the ground albedo it is not possible to reproduce the SZA dependency of the radiances.
- Systematic uncertainties of the actual measurement geometries. Sensitivity studies reveal that the differences between modeled and measured radiances can also be attributed to a slight misalignment of the telescope mounting.

The polarization, refraction and the CLD effect will be subject of future studies. However, the overall agreement of measurement and model for SZA up to 91° is fairly good, whereas for larger SZAs the modeled and measured radiances differ.

5.2. Self-consistency tests of particle optical property Jacobians

Jacobians of the radiances, actinic fluxes or light path integrals are validated using self-consistency tests. Their credibility relies on the validity of the quantities from which the Jacobians are derived, i.e. radiances and light path integrals (DOAS SCDs). SCDs are assumed to be correct since they can be obtained with the help of box air mass factors or the related absorption coefficient Jacobians of the logarithmic radiance (see [15]).

The applied self-consistency test consists of the following steps:

1. Systematic variation of a certain model parameter (e.g. a particles single scattering albedo or phase function moment).
2. Fit of a suitably flexible model function to the simulated quantity.
3. Comparison of the derivative of the fit model function with the Jacobians provided by the simulation.

Fig. 7 shows examples of these tests for Jacobians of the radiance and of the optical thickness τ of O_4, with respect to the aerosol extinction coefficient in the lowermost layer of the atmosphere $\varepsilon_{[0,0.1]km}$, the aerosol single scattering albedo ϖ_0 and the asymmetry parameter g. As indicated by the panels of Fig. 7, there is a reasonable agreement within the MC noise between the Jacobians predicted by the model and the polynomial derivatives. The deviations for the Jacobians dI_*/dg and $d\tau_{O_4}/d\varepsilon_{[0,0.1]km}$ can be explained by insufficient fitness (flexibility) of the polynomials used for the test. Nevertheless it appears that the predicted Jacobians are unbiased.

5.3. I3RC test case 4

Next we inter compare McArtim's predictions with corresponding simulations of other RT models for cases of the I3RC [37]. In the second phase of the I3RC certain radiative characteristics of a field of cumulus (Cu) clouds are compared. The clouds are represented by their optical properties at the wavelength 670 nm. A single phase function (approximated with 180 Legendre moments) and a single ϖ_0 are assumed. Extinction coefficients are given in form of a $100 \times 100 \times 36$ cell 3D field, extending over 6.67×6.67 km^2. The vertical cell height varies roughly between 200 m below 1 km, 40 m in the z range [1 km, 2.44 km] of the cloud field, and above 2.44 km coarser layer heights are assumed.

Here we compare top of the atmosphere (TOA) bidirectional reflectance (*BDR*) maps calculated by McArtim with

Please cite this article as: Deutschmann T, et al. The Monte Carlo atmospheric radiative transfer model McArtim: Introduction and validation of Jacobians and 3D features. JQSRT (2011), doi:10.1016/j.jqsrt.2010.12.009

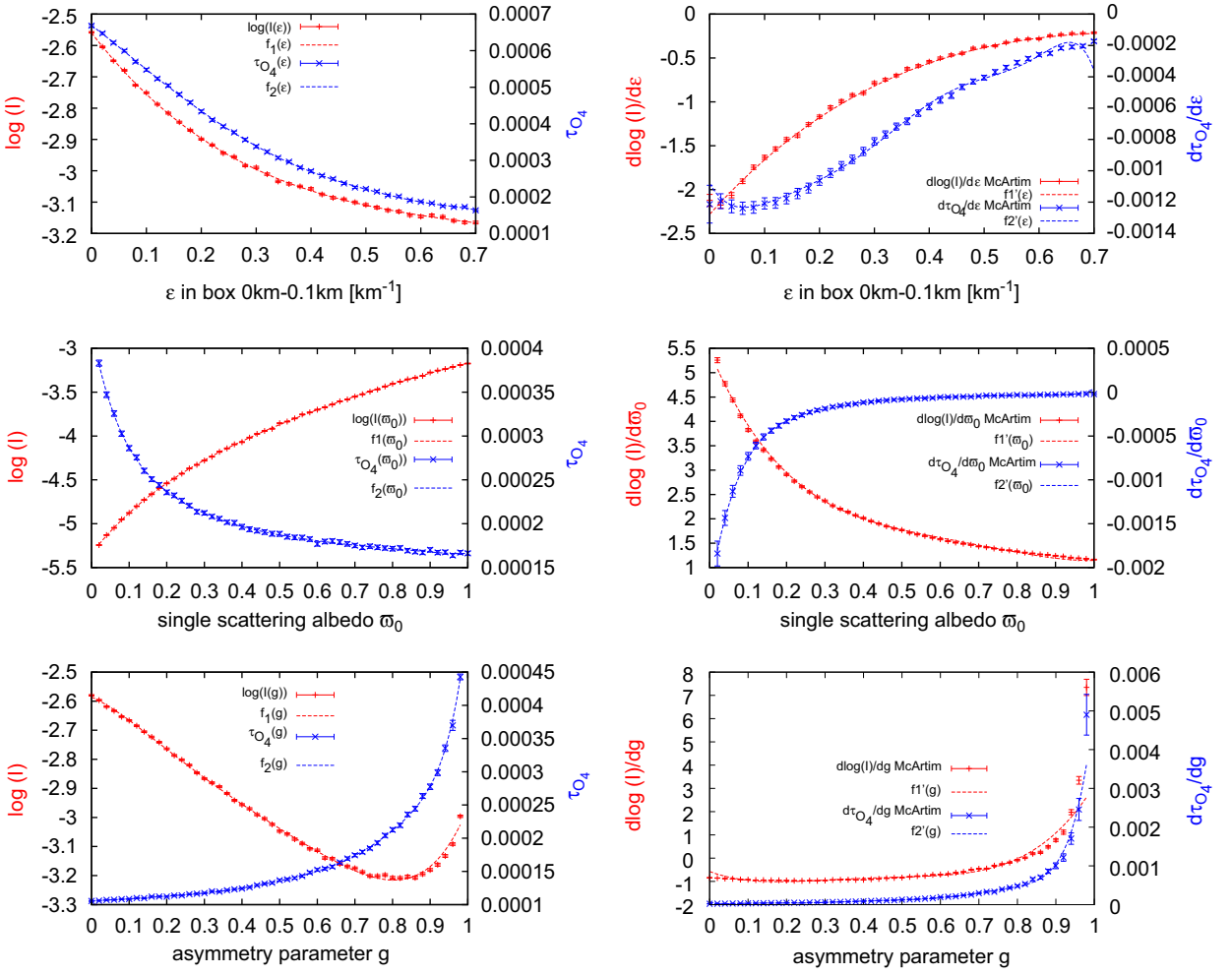

Fig. 7. Self-consistency test of aerosol property derivatives. Dependency of $\ln(I)$ (red) and τ_{O_4} (blue) on ε, ϖ_0 and g from top to bottom. The left side shows the dependency of $\ln(I)$ resp. τ_{O_4} on the aerosol property, the plots on right side show the respective derivatives. Model geometry: detector on the ground with 0.01° FOV looking 1° above the horizon, SZA=47° and RAA=223° $\lambda = 400$ nm. Crosses are model results, the curves on the left side are the fit polynomials whereas on the right side their derivatives $f'_{1|2}(x) = df_{1|2}/dx$ are shown. (For interpretation of the references to color in this figure legend, the reader is referred to the web version of this article.)

those of the I3RC models (second set, experiments 6 and 7), where the I3RC results consist of averaged results obtained from various unbiased RTM. The maps are obtained by setting a 0°FOV detector at 30 km altitude above each ground pixel of the map measuring in nadir direction as well as at a 60°zenith angle. Here, the *BDR* is defined as

$$\mathrm{BDR} = \frac{\pi I_{\mathrm{abs}}}{F_0 \mu_{\mathrm{SZA}}} = \frac{\pi I_*}{\mu_{\mathrm{SZA}}}, \tag{61}$$

where I_{abs} is the absolutely calibrated radiance, F_0 the extraterrestrial solar irradiance at TOA and μ_{SZA} is the cosine of the solar zenith angle.

The purple cloud shadows in the uppermost row in Fig. 8 attest to the fully 3D ray tracing capabilities of McArtim. In the middle column, the relative differences (ratios of the absolute deviations McArtim vs. I3RC and the I3RC BDRs) between the results of the I3RC models and McArtim are shown. The differences are dominated by Monte Carlo noise that only weakly correlates with the simulated radiance fields and seems to have a random nature. In the simulations carried out, the number of simulated trajectories is set to 10,000, which leads to standard deviations (assuming Gaussian noise) of between 4% and 50%. The variance of the estimated radiances strongly depends on the medium penetrated by the contributing photons, i.e. it significantly differs for cloudy and clear sky pixels. This could explain higher deviations especially in cloudy regions (Figs. 8 and 9) than for the cloud free regions. However, the noise signature seems to be only weakly correlated with the spatial extinction coefficient distribution. The recent study [67] demonstrates how the variance of radiances in the presence of clouds with strongly forward peaked phase functions can efficiently be reduced.

5.3.1. *Effective number of scatter events*

Plots of the effective number of scatter events are illustrative in order to demonstrate the versatility of the

Please cite this article as: Deutschmann T, et al. The Monte Carlo atmospheric radiative transfer model McArtim: Introduction and validation of Jacobians and 3D features. JQSRT (2011), doi:10.1016/j.jqsrt.2010.12.009

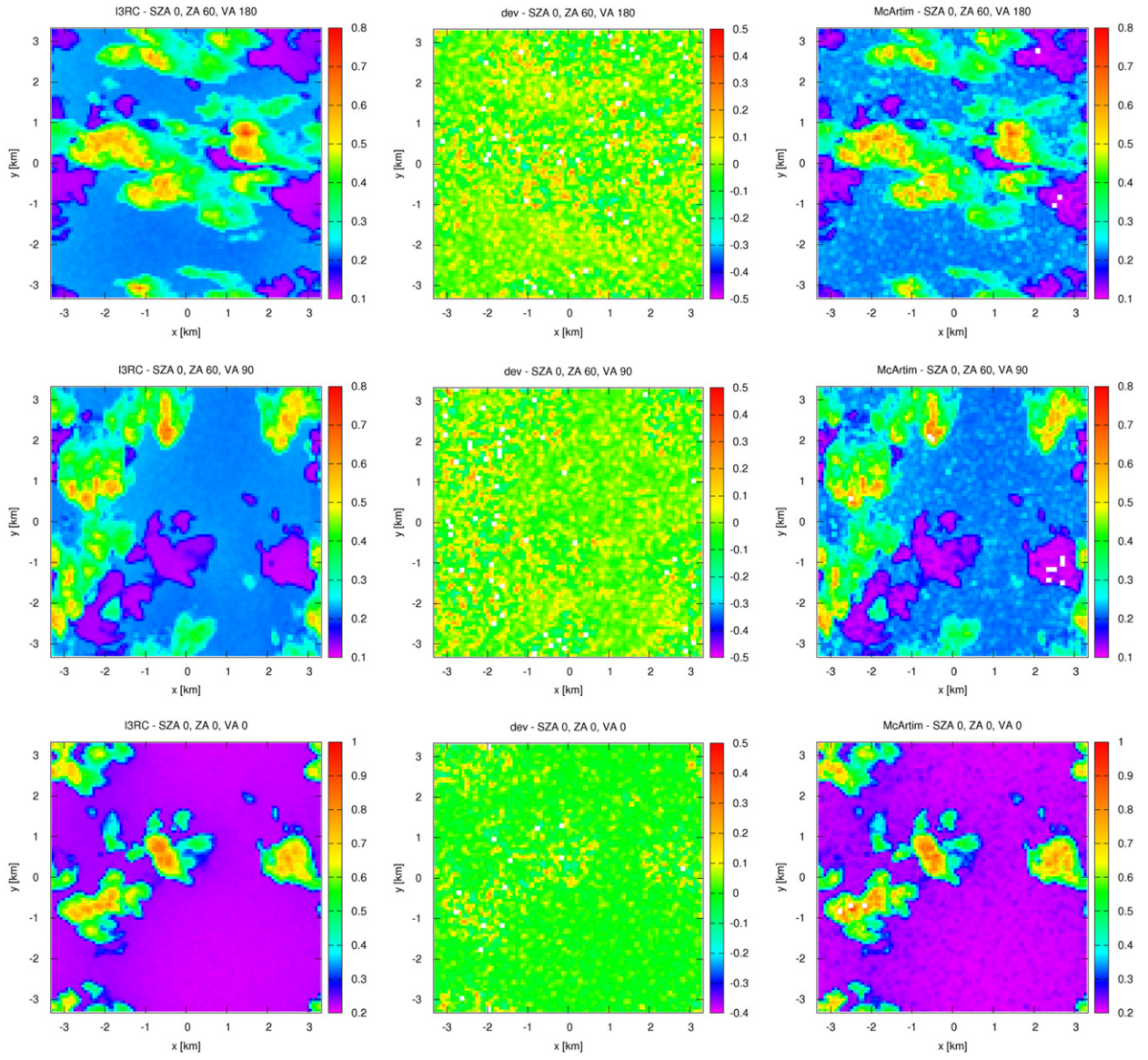

Fig. 8. Resulting BDR maps for the I3RC case 4, experiment 6 ($\lambda = 670$ nm). The cloud particle phase function has been approximated by Legendre polynomials to build look up tables. *Left panel column*: I3RC consensus results, *right panel column*: McArtim BDRs, *middle panel column*: relative difference McArtim vs. I3RC (see text). Model geometry: solar zenith angle (SZA) 0°, zenith angle (ZA) and viewing (azimuth) angle (VA) as shown in the captions of the respective plots.

Monte Carlo method. In the case of Rayleigh and rotational Raman scattering, ϖ_0 is unity. In Eq. (60) the $N_{p,n}$ are the number of scatter events of type x occurring in a trajectory sample of scatter order n.

Fig. 10 shows these quantities for the same geometries as in Fig. 8. In the first column the effective number of ground scattering events is shown. In cloud free regions, the result indicates that the photon trajectories undergo an average of roughly 1.4 ground scatter events. Below the clouds, the number approaches zero due to the cloud shielding. Thus, the sensitivity of the measured TOA radiances for ground properties is significantly decreased in cloudy compared to cloud free regions. The second column shows N_x for scattering by air molecules. As for scattering by aerosols (third column) in the vicinity of clouds, N_x is increased by a factor of roughly 2.5 as expected (see e.g. [68]). However, in absolute terms, the predominating scatter process is Mie scattering by cloud droplets as shown in the last column.

6. Conclusions

The present paper introduces the Monte Carlo radiative transfer model McArtim which is specifically designed for UV/vis/near IR remote sensing applications. Central to the McArtim code is to solve the integro-differential radiative

Please cite this article as: Deutschmann T, et al. The Monte Carlo atmospheric radiative transfer model McArtim: Introduction and validation of Jacobians and 3D features. JQSRT (2011), doi:10.1016/j.jqsrt.2010.12.009

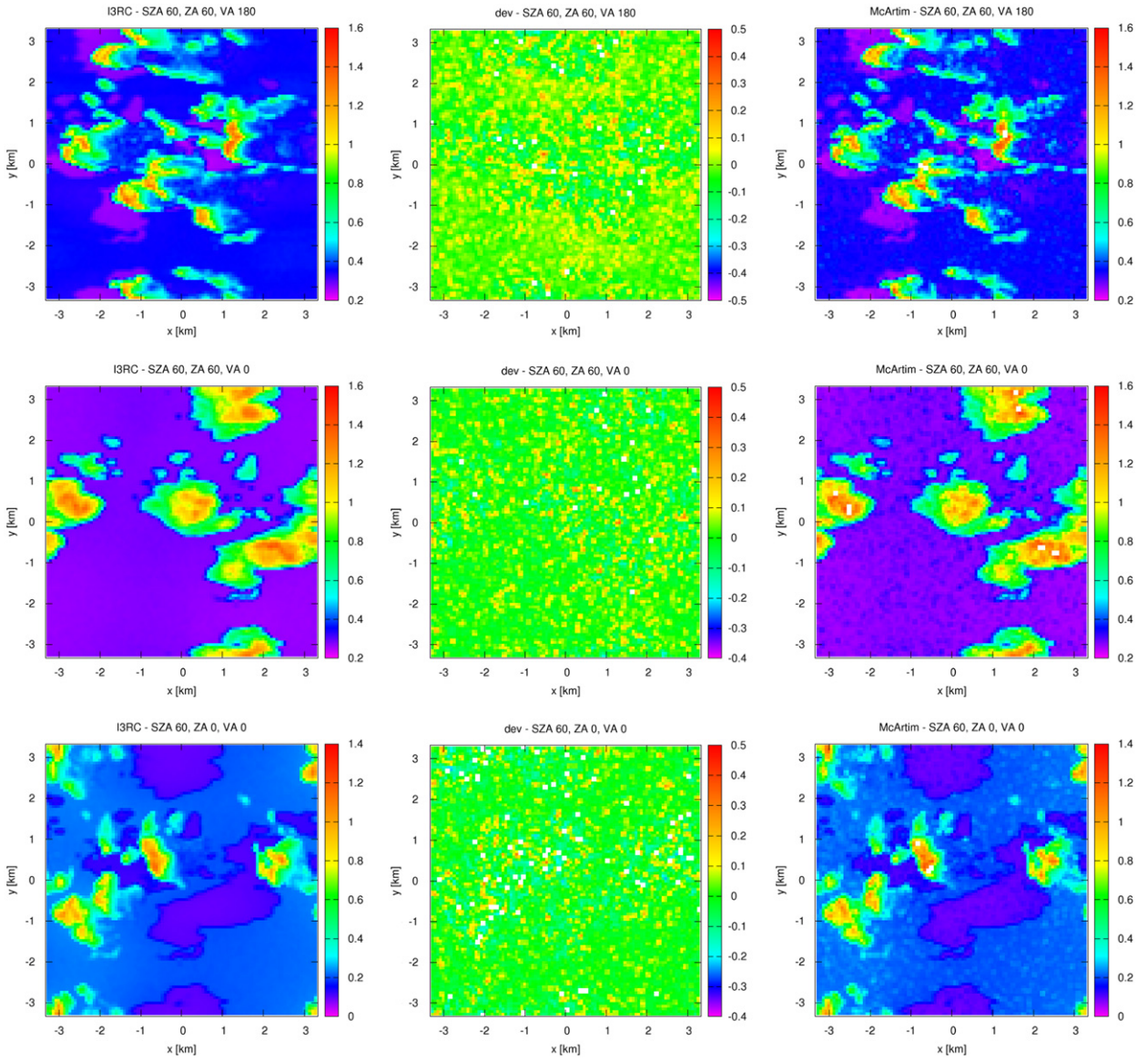

Fig. 9. Same as Fig. 8 but for SZA=60° and different viewing azimuth angles and zenith angles.

transfer equation (RTE) in terms of the so-called Neumann series, the summands of which are identified with the contributions of multiple scatter orders to the radiation field. It is shown how the adjoint formulation of the RTE can be utilized to calculate functionals of the radiation field.

By applying the Monte Carlo integration technique to the Neumann series, the core algorithm of each Monte Carlo RTM is found. The ray tracing method evolves from drawing samples of the integrals in the Neumann series and is at the same time the direct simulation of the photon transport process. In detail, the ray tracing consists in repeated simulation of the photon survival in extinction (i.e. scattering or absorption) events, sampling of scatter angles and free path lengths until the photon is absorbed or leaves the atmosphere at the TOA. The resulting trajectory is either an estimate of the radiation field in terms of the collision density or, employing the adjoint RTE formulation, an estimate of the so-called importance function associated to the characteristics (position, field of view, etc.) of a given detector.

Measurable radiometric quantities such as radiances, light path integrals, heating rates, actinic fluxes and Jacobians of these with respect to all relevant optical parameters are calculated from an ensemble of trajectories by local estimates and by the technique of dependent sampling. A specific advantage of dependent sampling is that Jacobians are simultaneously obtained from the analysis of a single trajectory ensemble. A drawback of this method is an increased variance of the calculated quantities.

Predictions of McArtim are validated with, cf. (a) intercomparison of measured and modeled radiances for large

Please cite this article as: Deutschmann T, et al. The Monte Carlo atmospheric radiative transfer model McArtim: Introduction and validation of Jacobians and 3D features. JQSRT (2011), doi:10.1016/j.jqsrt.2010.12.009

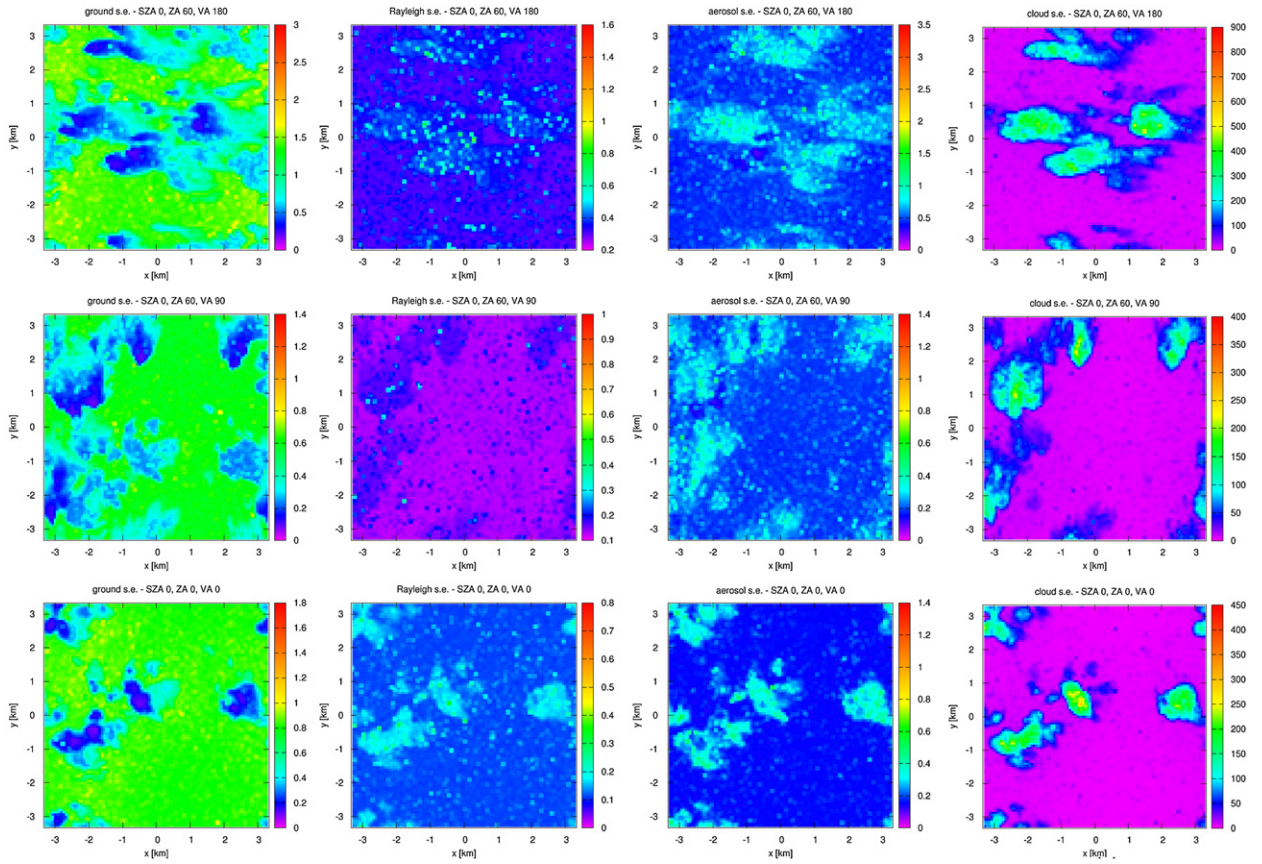

Fig. 10. Effective number of scatter events for the RT scenarios shown in Fig. 8. *First column*: ground scatter events (s.e.), *second column*: Rayleigh s.e., *third panel column*: aerosol s.e., *last column*: cloud s.e.

SZA's, the former being obtained from Limb observations of a balloon-borne spectrometer deployed into the stratosphere at high latitudes in late summer, (b) inter-comparison exercises of the I3RC project and (c) self-consistency tests which then rely on the validity of radiances. Theses validation exercises demonstrate that McArtim provides unbiased and exact results while being versatile and reasonably rapid in relevant RT applications.

Although Monte Carlo methods have a long tradition in RT modeling and are developed well, there remain still challenging tasks. For estimating Jacobians related to optical properties of aerosols or clouds, an algorithm to efficiently construct variance reduced estimates has to be found. There are several variance reduction methods such as the splitting technique or stratified sampling which are aimed to be included in the code. Another shortcoming of the present code is revealed in inter comparison exercises with measurements at large SZAs suggesting that more emphasis needs to be put on refraction and the Sun's Center to Limb darkening (CLD). In the current version of McArtim exact predictions are restricted to SZA lower or equal 90°. Furthermore, in order to extend the applicability range in future, the BRDF surface scattering model as well as a more sophisticated treatment of the rotational Raman scattering and, therewith, the simulation of polarization needs to be implemented in the code.

Acknowledgments

The first author would like to thank Dr. Alexander Marshak for giving a personal lecture on Monte Carlo radiative transfer modeling. We also want to thank Prof. Dr. Bernhard Mayer from the DLR for many interesting and fruitful discussions about Monte Carlo methods and Sanam Vardag for proof reading. Support of the study from the DFG Grant Pf-384-7 is highly appreciated. Finally we want to thank the reviewers for their enriching comments and suggestions.

References

[1] Chandrasekhar S. Radiative transfer. New York: Dover; 1960.
[2] Lathrop K. Use of discrete-ordinate methods for solution of photon transport problems. Nucl Sci Eng 1966;24:381–8.
[3] Fiveland W. Three-dimensional radiative transfer heat-transfer solutions by the discrete-ordinates method. J Thermophys Heat Transfer 1988;2:309–16.
[4] Stamnes K, Tsay S-C, Wiscombe W, Jayaweera K. Numerically stable algorithm for discrete-ordinate-method radiative transfer in multiple scattering and emitting layered media. Appl Opt 1988;27(12):2502–9.
[5] Metropolis N, Ulam S. The Monte Carlo method. J Am Stat Assoc 1949;44(247):335–41.
[6] Marchuk G, Mikhailov G, Nazaraliev M, Darbinyan R, Kargin B, Elepov B. Monte-Carlo method in atmospheric optics. Springer; 1976.
[7] Collins D, Blättner W, Wells M, Horak H. Backward Monte Carlo calculations of the polarization characteristics of the radiation

Please cite this article as: Deutschmann T, et al. The Monte Carlo atmospheric radiative transfer model McArtim: Introduction and validation of Jacobians and 3D features. JQSRT (2011), doi:10.1016/j.jqsrt.2010.12.009

emerging from spherical-shell atmospheres. Appl Opt 1972;11: 2684–96.
[8] Lenoble J. Radiative transfer in scattering and absorbing atmospheres: standard computional procedures. Hampton, VA: Deepak Publishing; 1985.
[9] Kattawar G, Adams C. Stokes vector calculations of the submarine light field in an atmosphere-ocean with scattering according to a rayleigh phase matrix: effect of interface refractive index on radiation and polarization. Am Soc Limnol Oceanogr 1989;34(8):1453–72.
[10] O'Hirok W, Gautier C. A three dimensional irradiative transfer model to investigate the solar radiation within a cloudy atmosphere. Part i: spatial effects. J Atmos Sci 1998;55:2162–79.
[11] Marshak A, Davis A. 3D radiative transfer in cloudy atmospheres. Springer; 2005.
[12] Iwabuchi H. Efficient Monte Carlo methods for radiative transfer modeling. J Atmos Sci 2006;63:2324–39.
[13] Mayer B. Radiative transfer in the cloudy atmosphere. Eur Phys J Conf 2009;1:75–99.
[14] Davis A, Marshak A. Solar radiation transport in the cloudy atmosphere: a 3d perspective on observations and climate impacts. Rep Progr Phys 2010;73 026801pp.
[15] Wagner T, Burrows J, Deutschmann T, Dix B, von Friedeburg C, Frieß U, et al. Comparison of box-air mass factors and radiances for multiple-axis differential optical absorption spectroscopy (max-DOAS) geometries calculated from different UV/visible radiative transfer models. Atmos Chem Phys 2007;7:1809–33.
[16] von Friedeburg C. Derivation of trace gas information combining differential optical absorption spectroscopy with radiative transfer modelling. PhD thesis, University of Heidelberg; 2003.
[17] Vlemmix T, Piters A, Stammes P, Wang P, Levelt P. Retrieval of tropospheric NO_2 using the max-DOAS method combined with relative intensity measurements for aerosol correction. Atmos Meas Tech 2010;3:2317–66.
[18] Prados-Román C, Butz A, Deutschmann T, Dorf M, Kritten L, Minikin A, et al. Airborne DOAS limb measurements of tropospheric trace gas profiles: case study on the profile retrieval of O_4 and bro. Atmos Meas Tech Discuss 2010;3:3925–69.
[19] Platt U. Differential optical absorption spectroscopy DOAS. Chem Anal Ser 1994;127:27–83.
[20] Platt U, Perner D. Measurements of atmospheric trace gases by long path differential UV/visible absorption spectroscopy. In: Optical and laser remote sensing. New York: Springer; 1983. p. 95–105.
[21] Platt U, Stutz J. Differential optical absorption spectroscopy: principles and application. Springer; 2008.
[22] Stutz J, Platt U. Numerical analysis and estimation of the statistical error of differential optical absorption spectroscopy measurements with least-squares methods. Appl Opt 1996;35:6041–53.
[23] Hönninger G, von Friedeburg C, Platt U. Multi axis differential optical absorption spectroscopy (max-DOAS). Atmos Chem Phys 2004;4: 231–54.
[24] Weidner F, Bösch H, Bovensmann H, Burrows J, Butz A, Camy-Peyret C, et al. Balloon borne limb profiling of UV/vis skylight radiances O3, NO2, and bro: technical set-up and validation of the method. Atmos Chem Phys 2005;5:1409–22.
[25] Kritten L, Butz A, Dorf M, Deutschmann T, Kühl S, Prados-Román C, Puķīte J, Rozanov A, Schofield R, Pfeilsticker K. Time dependent profile retrieval of UV/vis absorbing radicals from balloon-borne limb measurements—a case study on NO2 and O3. Atmos Meas Tech 2010;3:933–46.
[26] Pfeilsticker K. First geometrical path length probability density function derivation of skylight from high-resolution oxygen a-band spectroscopy. 2. Derivation of the Lévy index for the skylight transmitted by midlatitude clouds. J Geophys Res 1999;104:4101–16.
[27] Funk O. Photon pathlengths distributions for cloudy skies—oxygen a-band measurements and radiative transfer model calculations. PhD thesis, University of Heidelberg; 2000.
[28] Scholl T. Photon path length distributions for cloudy skies—their first and second-order moments inferred from high resolution oxygen a-band spectroscopy. PhD thesis, University of Heidelberg; 2006.
[29] Pfeilsticker K, Erle F, Funk O, Veitel H, Platt U. First geometrical path lengths probability density function derivation of the skylight from spectroscopically highly resolving oxygen a band observations. 1. Measurement technique, atmospheric observations, and model calculations. J Geophys Res 1998;103:11483–504.
[30] Wagner T, Dix B, von Friedeburg C, Frieß U, Sanghavi S, Sinreich R, et al. Max-DOAS O4 measurements: a new technique to derive information on atmospheric aerosols—principles and information content. J Geophys Res 2004;109:D22205.
[31] Frieß U, Monks JRP, Rozanov RSA, Platt U, Wagner T. Max-DOAS O4 measurements: a new technique to derive information on atmospheric aerosols: 2. Modeling studies. J Geophys Res 2006;111: D14203.
[32] Irie H, Kanaya Y, Akimoto H, Iwabuchi H, Shimizu A, Aoki K. Dual-wavelength aerosol vertical profile measurements by max-DOAS at Tsukuba, Japan. Atmos Chem Phys 2009;9:2741–9.
[33] Li X, Brauers T, Shao M, Garland R, Wagner T, Deutschmann T, et al. Max-DOAS measurements in southern china: retrieval of aerosol extinctions and validation using ground-based in situ data. Atmos Chem Phys 2010;10:2079–89.
[34] Kattawar G, Plass G. Radiance and polarization of multiple scattered light from haze and clouds. Appl Opt 1967;7(8):1519–27.
[35] Cornet C, Szczap F, C-Labonnote L. Three-dimensional polarized Monte Carlo atmospheric radiative transfer model (3dmcpol): 3d effects on polarized visible reflectances of a cirrus cloud. J Quant Spectrom Radiat Transfer 2010;111:174–86.
[36] Emde C, Buras R, Mayer B, Blumthaler M. The impact of aerosols on polarized sky radiance: model development, validation and applications. Atmos Chem Phys 2010;10:383–96.
[37] Cahalan R, Oreopoulos L, Marshak A, Evans K, Davis A, Pincus R, et al. The international intercomparison of 3d radiation codes (i3rc): bringing together the most advanced radiative transfer tools for cloudy atmospheres. Bull Am Meteorol Soc 2005;86(9):1275–93.
[38] Pincus R, Evans K. Computational cost and accuracy in calculating three dimensional radiative transfer: results for new implementations of Monte Carlo and SHDOM. J Atmos Sci 2009;66:3131–46.
[39] Mishchenko M. Vector radiative transfer equation for arbitrarily shaped and arbitrarily oriented particles: a microphysical derivation from statistical electromagnetics. Appl Opt 2002;41:7114–34.
[40] Mishchenko M. Microphysical approach to polarized radiative transfer: extension to the case of an external observation point. Appl Opt 2003;42:4963–7.
[41] Mishchenko M, Travis L, Lacis A. Multiple scattering of light by particles: radiative transfer and coherent backscattering. Cambridge University Press; 2006.
[42] Lacis A, Chowdhary J, Mishchenko M, Cairns B. Modeling errors in diffuse-sky radiation: vector vs scalar treatment. Geophys Res Lett 1998;25:135–8.
[43] Mishchenko M. Gustav Mie and the fundamental concept of electromagnetic scattering by particles: a perspective. J Quant Spectrom Radiat Transfer 2009;110:1210–22.
[44] Vountas M, Rozanov V, Burrows J. Ring effect: impact of rotational raman scattering on radiative transfer in Earths atmosphere. J Quant Spectrom Radiat Transfer 1998;60(6):943–61.
[45] Dorny N. Script on linear differential operators. Technical Report, University of Pennsylvania, 〈www.seas.upenn.edu/dorny/VectorSp/diffoperatorsp93-143.pdf〉; 2002.
[46] Vladimirov V. Mathematical problems of the single-velocity theory of particle transfer. Tr Mat Inst Akad Nauk SSSR 1961;61:157.
[47] Caballero. Existence of solutions of an integral equation Chandrasekhar type in the theory of radiative transfer. Electron J Diff Eqn 2006;57:1–11 ISSN: 1072-6691.
[48] Kahn H. Random sampling (Monte Carlo) techniques in neutron attenuation problems. Nucleonics 6(5,6):1950.
[49] Ciddor P. Refractive index of air: new equations for the visible and near infrared. Appl Opt 1996;35:1566–73.
[50] Penndorf R. Tables of the refractive index for standard air and the rayleigh scattering coefficient for the spectral region between 0.2 and 200 μm and their application to atmospheric optics. Opt Soc Am 1957;47(2):176–82.
[51] Shefov N. Spectroscopic, photoelectric, and radar investigations of the aurora and the nightglow. Izd Akad Nauk 1:1959.
[52] Grainger J, Ring J. Anomalous Fraunhofer line profiles. Nat Lond 1962;193 762 pp.
[53] Kattawar G, Young A, Humphreys T. Inelastic scattering in planetary atmospheres i. The ring effect without aerosols. J Astrophys 1981;243(3):1049–57.
[54] Bussemer M. Der ring effekt: ursachen und einfluss auf die spektrokopische messung stratosphärischer spurenstoffe. Master's thesis, University of Heidelberg; 1993.
[55] Chance K, Spurr R. Ring effect studies: Rayleigh scattering, including molecular parameters for rotational raman scattering, and the Fraunhofer spectrum. Appl Opt 1997;36:5224–30.
[56] Landgraf J, Hasekamp O, van Deelen R, Aben I. Rotational raman scattering of polarized light in the earth atmosphere: a vector radiative transfer model using the radiative transfer perturbation theory approach. J Quant Spectrom Radiat Transfer 2004;87: 399–433.

Please cite this article as: Deutschmann T, et al. The Monte Carlo atmospheric radiative transfer model McArtim: Introduction and validation of Jacobians and 3D features. JQSRT (2011), doi:10.1016/j.jqsrt.2010.12.009

[57] Wagner T, Beirle S, Deutschmann T. Three-dimensional simulation of the ring effect in observations of scattered sun light using Monte Carlo radiative transfer models. Atmos Meas Tech 2009;2: 113–24.
[58] Wiscombe W. Mie scattering calculations: advances in technique and fast, vector-speed computer codes. Technical Note, NCAR; 1979.
[59] Rothman L, Jacquemart D, Barbe A, Benner D, Birk M, Brown L, et al. The Hitran 2004 molecular spectroscopic database. J Quant Spectrom Radiat Transfer 96(2):2005.
[60] Frankenberg C. Retrieval of methane and carbon monoxide using near infrared spectra recorded by Sciamachy onboard Envisat, algorithm development and data analysis. PhD thesis, University of Heidelberg; 2004.
[61] Goody R, Yung Y. Atmospheric radiation—theoretical basis. Oxford University Press; 1989.
[62] Bates D. Rayleigh scattering by air. Planet Space Sci 1984;32(6): 785–90.
[63] Mayer B, Hoch S, Whiteman C. Validating the mystic three-dimensional radiative transfer model with observations from the complex topography of Arizona's meteor crater. Atmos Chem Phys 2010;10: 8685–96.
[64] Puķīte J, Kühl S, Deutschmann T, Platt U. Accounting for the effect of horizontal gradients in limb measurements of scattered sunlight. Atmos Chem Phys 2008;8:3045–60.
[65] Kern C, Deutschmann T, Vogel L, Wöhrbach M, Wagner T, Platt U. Radiative transfer corrections for accurate spectroscopic measurements of volcanic gas emissions. Bull Volcanol 2010;72:233–47.
[66] Bösch H, Camy-Peyret C, Chipperfield M, Fitzenberger R, Harder H, Platt U, et al. Upper limits of stratospheric io and oio inferred from center-to-limb-darkening-corrected balloon borne solar occultation visible spectra; implications for total gaseous iodine and stratospheric ozone. J Geophys Res 2003;108 445pp.
[67] Buras R, Mayer B. Efficient unbiased variance reduction techniques for Monte Carlo simulations of radiative transfer in cloudy atmospheres: the solution. J Quant Spectrom Radiat Transfer 2010;112: 434–47.
[68] Marshak A, Wen Jr GJC, Remer L, Loeb N, Cahalan R. A simple model for the cloud adjacency effect and the apparent bluing of aerosols near clouds. J Geophys Res 2008;113:D14S17.

Please cite this article as: Deutschmann T, et al. The Monte Carlo atmospheric radiative transfer model McArtim: Introduction and validation of Jacobians and 3D features. JQSRT (2011), doi:10.1016/j.jqsrt.2010.12.009